ASSESSING THE ACCURACY OF VERTICAL PROFILES OF HEATING AND VERTICAL MOTION IN THE TROPICAL EASTERN PACIFIC

A Thesis

by

KEITH CHRISTOPHER WHITE

Submitted to the Office of Graduate and Professional Studies of
Texas A&M University
in partial fulfillment of the requirements for the degree of

MASTER OF SCIENCE

Chair of Committee,	Courtney Schumacher
Committee Members,	Robert Korty
	Christopher Nowotarski
	Benjamin Giese
Head of Department,	Ping Yang

December 2015

Major Subject: Atmospheric Sciences

ABSTRACT

Vertical profiles of heating (Q_1) are a result of the interaction between radiative heating, eddy sensible heat transport, and latent heating from cloud and precipitation systems. The third component is the largest by an order of magnitude in deep convective regions like the intertropical convergence zone (ITCZ). Vertical motion (ω) is often used as a proxy for Q_1 and, in regions lacking in situ observations, ω profiles from model reanalyses are commonly used to make inferences about large-scale circulations and climate sensitivity. In the East Pacific (EP) ITCZ, ω profiles exhibit large variability between reanalyses and have a bottom-heavy shape centered near 800 hPa that contrasts with the 400 hPa peak in the West Pacific (WP) warm pool. Rainfall between the two regions is similar; however, stratiform rain fractions are higher in the EP than the WP, and the low-level ω peak in the profiles persists even during El Niño, when precipitation systems become similar between the two regions. These facts all point towards erroneous reanalysis profiles in the EP.

Echo statistics from the Tropical Rainfall Measuring Mission (TRMM) Precipitation Radar (PR) and the Dual-frequency Precipitation Radar (DPR) aboard the Global Precipitation Measurement (GPM) satellite are examined across the tropical Pacific. The DPR K_u-band is more sensitive to upper level, low-reflectivity cloud and sees more near-surface echo than the PR, but the overall echo statistics are generally similar. The addition of the DPR K_a-band high sensitivity scans further enhances the DPR sensitivity to upper level cloud, but echo statistics are still not substantially different than TRMM. Utilizing the 16-year TRMM climatology for increased sampling,

previously known differences in convection between the EP and WP are confirmed, but they aren't great enough to justify such a large discrepancy in reanalysis ω profiles.

The relationships between Q_1 and ω to rainfall statistics in select tropical field campaigns are also investigated. In all cases, the magnitude and height of the peak values of each variable increase with increasing stratiform rain fraction, further suggesting that the EP should have top-heavy rather than bottom-heavy heating and ω because of its higher stratiform rain fraction.

ACKNOWLEDGEMENTS

First, I'd like to acknowledge my incredible advisor and role model, Dr. Courtney Schumacher. I am very fortunate to have Courtney as my committee chair, for more reasons than I could fit on this page. In addition to helping shape me into a good scientist, her kind and outgoing attitude made me feel not like a student, but a friend, and without her guidance none of this would be possible. Aaron Funk did a lot of the pre-processing of the data used in this work and provided a few figures. He's also been awesome at communicating with me through email over the past 2 years, which has been integral to my completion of this work.

Thanks also to my committee members, Dr. Nowotarski, Dr. Korty, and Dr. Giese, for their help throughout the process and their thoughts on this work, and to Dr. Conlee for allowing me to help out with Practical Weather Forecasting and put my head in the future clouds occasionally instead of the past ones.

To Chris, Kyle, Jack, and Hannah: Your friendship has been more valuable to me than my words can muster. Extra appreciation goes to Kyle for being my go-to guy for pretty much anything. I'd like to thank all of my other friends and colleagues and the department faculty and staff for making my time at Texas A&M University a great experience. I also want to extend my gratitude to the National Aeronautics and Space Administration, which provided the funding and much of the data for this research.

Finally, a gigantic thank you to Amy, for the sacrifices she's made, the support she's given, but most importantly, for always being at my side.

TABLE OF CONTENTS

Page

LIST OF FIGURES

Page

1. INTRODUCTION

Meteorological hypotheses are usually advanced through one or more of the following three methods: observational evidence, modeling results, or theory and mathematical proof. To obtain a "real-world" answer, meteorologists typically rely on observational evidence. But collecting meteorological data over the vast open oceans has always proven difficult. This is especially true over the tropical eastern Pacific (EP) where there are few to no islands for thousands of kilometers. The majority of cloud and precipitation data collected in the EP is remotely sensed by satellites (Tropical Rainfall Measuring Mission (TRMM), Global Precipitation Measurement (GPM), CloudSat, etc.), with in situ data only available during short field campaigns, e.g., the Tropical Eastern Pacific Process Study, which took place in August 1997 (TEPPS; Yuter and Houze 2000) and the September/October 2001 East Pacific Investigation of Climate Processes in the Coupled Ocean-Atmosphere System (EPIC; Raymond et al. 2004). Owing to the dearth of in situ observations over regions like this, there is a reliance on atmospheric reanalysis data to fill in the gaps. Unfortunately, reanalyses are largely model-based over the open ocean and thus are subject to errors that are often apparent in parameterizations of small-scale processes. Despite their shortcomings, present literature utilizes reanalyses as truth in regions lacking true observations, including the EP.

Vertical motion (ω) is one of the key output variables in reanalysis datasets due to its relationship to the formation of cloud and precipitation systems and the dynamical responses induced by them. However, a pressing question in the EP is a large discrepancy between data sets regarding vertical profiles of ω and heating (Q_1). Figure 1

shows ω profiles from eight reanalyses (described further in Stachnik and Schumacher (2011)) for the West and East Pacific. The geographical boxes chosen for Figure 1 are of equal size: 140-160 ˚E, 5-7.5 ˚N for the western Pacific (WP) and 120-140 ˚W, 7.5-10 ˚N for the EP, since the ITCZ shifts poleward there (see Figure 5). These regions are the same as those used in Back and Bretherton (2006) and cover areas with comparable total rain amounts (there is 18.2% more rain in the WP) that experience frequent active deep convection. However, there is large variability in the peak magnitude of mean vertical motion profiles in the EP intertropical convergence zone (ITCZ) ranging from -0.02 to -0.1 Pa/s among the eight reanalyses (Figure 1, right), as well as a bottom-heavy shape that contrasts with the top-heavy and less variable profile in the WP warm pool (Figure 1, left). The difference in the shape of the profiles suggests fundamentally different cloud and precipitation systems between the regions. The same eight reanalyses will be used in this research, and additional details about them can be found in section 2.1.

Tropical precipitation is often separated into two types: convective or stratiform (Houze 1997). Cumulus or cumulonimbus clouds produce convective rain, while stratiform rain typically falls out of nimbostratus clouds at mid- and upper levels as ice and melts once it reaches an above-freezing layer. In the tropics, some drizzle or light rain can fall from stratus or stratocumulus with cloud tops below the 0˚C isotherm, but within the ITCZ, this amount is negligibly small (Schumacher and Houze 2003b)

Each precipitation type can be defined based on the local values of ω. When the vertical velocity of an air parcel in the mid to upper troposphere is large enough to maintain supersaturation, but less than the terminal fall velocity of ice crystals and snow

within (e.g., 0.5 m/s), water vapor will be deposited onto the ice crystals over time (Houze 1993). This, along with ice crystal aggregation, is the primary mechanism of stratiform rain growth. Vertical velocities are much larger in convective clouds, typically around 1-10 m s^{-1}, and growth of hydrometeors comes mainly via collision and coalescence below the 0ºC level and riming aloft. This process occurs on a much faster timescale than stratiform precipitation, but also on smaller spatial scales. A typical convective updraft is on the order of one kilometer in width, while stratiform regions can span tens to perhaps hundreds of kilometers. Although these precipitation types are a result of fundamentally different growth processes, they are often simultaneously ongoing in deep convective systems.

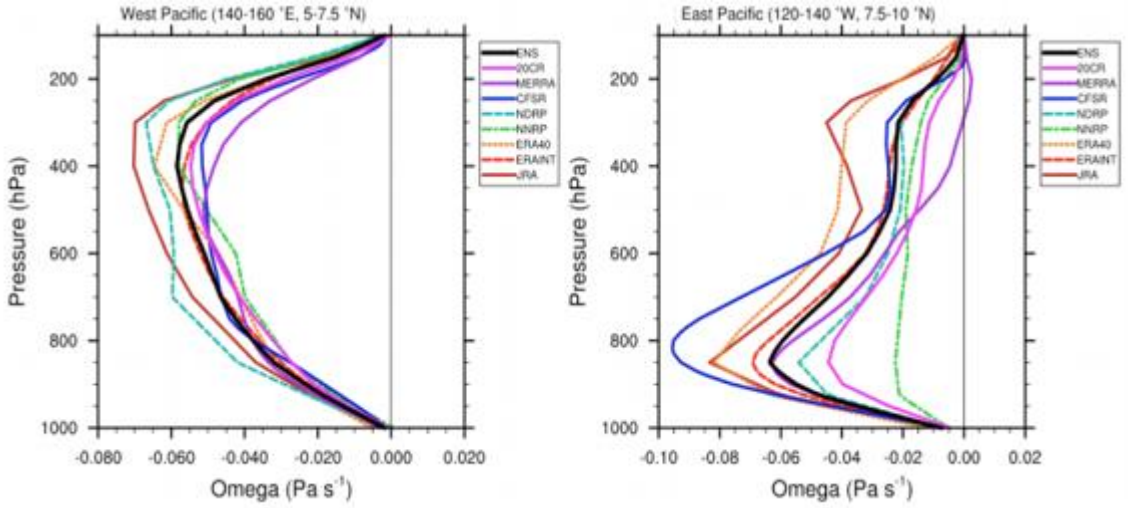

Figure 1 – Annual Average pressure velocity for 1979-2008 for eight reanalyses over the west (left) and east Pacific Ocean (right). The ensemble average is indicated by the black line.

Profiles of Q_1 are a result of the interaction between radiative heating, eddy sensible heat transport, and latent heating from cloud and precipitation systems (Yanai et

al. 1973), the latter of which is an order of magnitude larger than the other two components in deep convective regions (Houze 1982). Since large-scale, upward vertical motion leads to the development of clouds and precipitation, ω profiles should be the dominant factor in diabatic heating in deep convective, rainy regions like the ITCZ (Mapes and Houze 1995; Back and Bretherton 2006; Wong et al. 2014). Because heating is difficult, if not impossible, to measure directly, vertical motion is often used as a proxy.

The relationship between Q_1 and ω was further confirmed by Takayabu et al. (2010), who emphasized that deep systems and congestus are the two dominant modes of non-drizzle precipitation over tropical oceans. Similar to this finding, Zhang and Hagos (2009) performed a rotational empirical orthogonal function analysis in order to determine the leading modes of variance in the Q_1 profiles from nine tropical field campaigns. The two leading modes, one shallow and one deep, explain 85% of the variance. When one campaign is removed from the data, the variance explained by the two modes increases to 93% (Hagos et al. 2010). These leading modes led to the identification of two (or sometimes three) large-scale heating structures, which correlate with the precipitation types defined above: stratiform heating with a peak near 400 hPa and cooling near 700 hPa and convective heating with one singular heating maximum near 700 hPa (with the third being a deeper convective profile centered higher, near 400 hPa). The cooling at lower levels in stratiform systems is the result of melting and evaporation of particles as they fall through warm, dry air beneath the mid-level cloud

base. Variations in the fractional contributions of these "building blocks" account for the evolution of the large-scale mean heating profile (Mapes et al. 2006; Hagos 2010).

Comparatively, three "idealized" latent heating profiles (the dominant heating component in Q_1) were created by Schumacher et al. (2004), and were assigned to individual TRMM radar pixels (dimensions of ~4.3 to 5 km in the horizontal at nadir, increasing outward, and 250 m in the vertical) of stratiform, deep convective and shallow convective precipitation. These profiles can be seen in Figure 2, along with the heating profiles derived from different fractions of each precipitation type. Idealized ω profiles would look very similar given their close relationship to each other. It is apparent that higher stratiform rain fractions lead to higher peaks in latent heating, and since higher stratiform rain fractions are observed in convectively active portions of the EP than in the WP (Schumacher and Houze 2003a), we would expect a higher peak in latent heating (and thus vertical motion) in the EP (Schumacher et al. 2004).

Observations from the TEPPS and EPIC field campaigns (Cifelli et al. 2007) as well as from satellites (Masunaga et al. 2005; Takayabu et al. 2010) agree that while the EP sees many more shallow precipitation systems and congestus than the WP, deep convection still regularly occurs in the EP. It is usually associated with synoptic-scale waves including, but not limited to, eastward-moving equatorial Kelvin waves (Straub and Kiladis 2002) and westward-moving easterly waves (Serra and Houze 2002; Peterson et al. 2003). Sounding observations from the Kwajalein experiment (KWAJEX) in the west-central Pacific have shown that cooling occurs through most of the atmosphere in the ridge phase of easterly waves, with heating at low levels during the

pre-trough, increasing in height through the post-trough region as precipitation transitions from convective to stratiform (Schumacher et al. 2007).

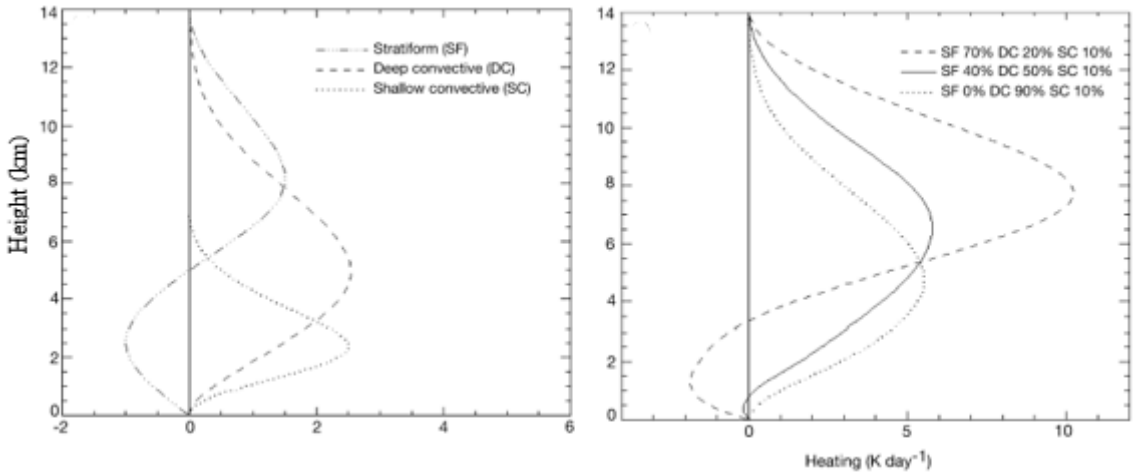

Figure 2 – Three idealized heating profiles (left). The x axis is nondimensional until a precipitation amount is given. Total latent heating profiles for 0, 40, and 70% stratiform rain fractions, assuming 3.5 m/yr of rain (right). From Schumacher et al. (2004).

Much of the rain in the tropics falls from mesoscale convective systems (MCSs) forced by the aforementioned waves (Roca et al. 2014). Three quarters of all rain comes from systems with durations longer than 12 hours, and 60% comes from systems that travel distances longer than 250 km. These systems primarily occur near 10 ˚N in the EP, especially during boreal summer (Nesbitt et al. 2000), which is why the tropical rain belt associated with the ITCZ is shifted further north relative to the WP.

There are numerous methods for estimating rainfall from satellites, even just from the TRMM satellite itself. On board are the TRMM Microwave Imager (TMI) and the Precipitation Radar (PR). The TMI is a passive sensor, while the PR is active, but

precipitation is estimated from the retrievals of both instruments. These two instruments produce similar rainfall estimates over the WP, however the PR algorithm seems to underestimate rainfall in the EP relative to the TMI (Shige et al. 2008b). Comparisons of observed brightness temperatures to simulated values from a radiative transfer model using PR rainfall estimates display larger differences in the EP than the WP. The prevailing hypothesis is that the discrepancy is caused by more maritime drop size distributions (DSDs) in the EP than the WP DSDs used in the PR algorithm.

Estimates of latent heating can also be calculated from TRMM retrievals in a number of ways. The spectral latent heating (SLH) algorithm, which uses only PR data, and the convective-stratiform heating (CSH) algorithm that uses both the TMI and PR are used most often. There are also the precipitation radar heating (PRH) algorithm, and a TMI-based training algorithm (TRAIN). Some advantages and disadvantages of each were discussed in Tao et al. (2006), and improvements were made to the SLH and CSH algorithms in the years following (Shige et al. 2007, 2008a, 2009; Tao et al. 2010). Further discussion of the TRAIN algorithm will not be necessary, as it is not very accurate over our region of interest due to the abundance of shallow precipitation (Grecu et al. 2009).

The PRH algorithm has been shown to represent stratiform cooling in the lower troposphere well over the Atlantic, but heating does not increase in height with increasing precipitation rate (Hagos et al. 2010). Short and Nakamura (2000) showed a correlation between PR echo top height and rain rate of 0.71, so this algorithm is also unsatisfactory.

The CSH algorithm was developed in the early to mid-1990s, before the launch of TRMM (Tao et al. 1993). In an early study of latent heating profiles derived from TRMM, Tao et al. (2001) showed that the CSH algorithm underestimated heating, suffering from the underestimation of rain by the PR in relation to the TMI. Chan and Nigam (2009) also found that the CSH retrieval was weak in comparison to other products by as much as a factor of two. Nonetheless, the CSH latent heating profiles agreed well with diagnostic budget studies in that they have a singular peak heating level. Improvements to this method (Tao et al. 2010) led to a larger heating maximum about 1 km lower and a significant increase in low- and mid-level heating, however a majority of the change is attributable to systems over land.

Shige et al. (2004) developed the SLH method, which uses lookup tables that refer to precipitation top height for convective and shallow rain, but for anvil rain it refers to precipitation rate at the melting level. This allows for the calculation of heating even in periods of no surface rain. Improvements were made in Shige et al. (2007), including separating convective heating into upper level ice and lower level liquid water processes and comparing lookup tables for observed melting level to data from the Tropical Ocean and Global Atmosphere Coupled Ocean-Atmosphere Response Experiment (TOGA-COARE) to better assign heights for stratiform heating aloft and cooling below.

Shige et al. (2007) compared SLH heating profiles to those calculated from the CSH algorithm for various regions in February of 1998 and 1999. They use Q_1-Q_r (where Q_r is the radiative heating) as an approximation for latent heating, ignoring eddy

sensible heat fluxes that cannot be sampled by satellite. In the EP in February 1998 (which was during a strong El Niño), the SLH profile appears top-heavy, with a peak between 7-8 km of about 2.5 K/day. There is also a secondary peak near 2 km that is not resolved well in the CSH algorithm. Overall, the profile is very similar to that in the WP, while the central Pacific has a stronger heating peak of 4-4.5 K/day. In February 1999, heating is confined to a small peak just below 2 km in the SLH profile in the EP, while the CSH has a broader, weaker peak closer to 3 km. Trade cumuli in the EP are typically capped at the top of the boundary layer, just below the return flow of the shallow meridional circulation (SMC; Zhang et al. 2004), so the SLH algorithm is likely more accurate for statistical analysis. The large differences in heating between El Niño/Southern Oscillation (ENSO) periods may be attributable in part to the region chosen, which extends well into the cold tongue in the Southern Hemisphere.

Another study using Q_1-Q_r estimates of latent heating from the SLH algorithm mapped the values across the tropical Pacific at 2 km and 7.5 km as well as the ratio (2 km/7 km; Takayabu et al. 2010, their Fig. 10). At both altitudes, latent heating is slightly stronger in the EP ITCZ than the WP warm pool, leading to a similar ratio in both regions. Values of ω at 500 hPa are also shown, and appear similar, although there are some stronger values from 150-160 ºE and 5-7.5 ºN in the WP.

Hagos et al. (2010) performed a comparison of reanalysis heating versus heating retrieved from the various satellite algorithms defined above (Figure 3), finding a more top-heavy profile of heating in the EP (right) derived from the satellite algorithms (dashed lines) than from reanalysis datasets (solid lines), reinforcing the discrepancy. It

is important to note that the satellite retrieval algorithms also show variability in the height and magnitude of peak heating, but every satellite heating algorithm has a higher peak than each reanalysis in their study.

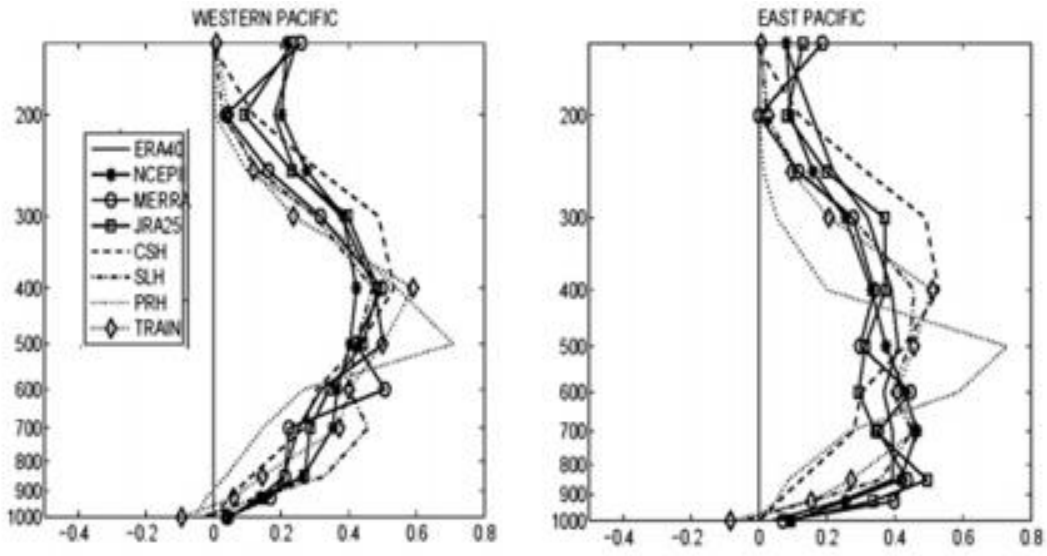

Figure 3 – Normalized profiles of heating for the WP (left) and EP (right). Data comes from reanalyses (ERA40, NCEPII, MERRA, JRA25) and satellite retrieval algorithms (CSH, SLH, PRH, TRAIN). From Hagos et al. (2010).

Profiles of heating in the Community Climate Model, version 3 (CCM3; Nigam et al. 2000), had an even more bottom-heavy heating profile than reanalyses. In a companion paper, Nigam and Chung (2000) showed that zonal wind errors in that model can be attributed in large part to faulty vertical heating profiles, emphasizing the importance of accurately representing them.

Non-precipitating clouds can also impact heating profiles. A primitive budget study from the Barbados Oceanographic and Meteorological Experiment (BOMEX) separated the campaign into a disturbed and an undisturbed period (Nitta and Esbensen

1974). During the undisturbed period, average ω was positive (downward motion) throughout the atmosphere, with weakly positive Q_1 in the lowest 100 hPa and negative Q_1 above, with a peak near the top of the trade wind inversion where detrainment occurs. Throughout the disturbed period, negative ω was found in the lowest 100 hPa, with weaker positive ω aloft. Positive Q_1 occupied a layer 200 hPa deep, with weakly negative heating above. Detrainment begins about 350 hPa above the surface in the disturbed period.

More recently, budgets were calculated for individual cloud types. Schumacher et al. (2008) separated cloud observations from KWAJEX into low (<800 hPa), medium (800-400 hPa), and high (>400 hPa) based clouds. They were further separated into 10 different types for each height bin, with rain rates and frequencies of occurrence listed. The non-raining and lightly raining cloud types generally exhibit a minimum in Q_1 near -2 K/day in the mid-troposphere likely due to large-scale radiative cooling. Moderately raining types in contrast have positive peaks in heating of 2-4 K/day in the low- and mid-troposphere. Positive heating peaks of 10-15 K/day in the mid- to upper troposphere are found in the heavily raining cloud types. In a study of 10 different tropical and subtropical field campaigns, Stachnik et al. (2013) separated clouds by International Satellite Cloud Climatology Project (ISCCP) weather states. While there is significant spread in the data, on average the cumulus weather state exhibits a low level peak in Q_1 near 1 K/day. For the weather states that rain more heavily, the Q_1 profiles are strongly positive. The above evidence points towards a relatively small contribution to latent heating from non-precipitating or weakly precipitating cloud.

Studies using the sensitive cloud profiling radar aboard CloudSat have shown there are 2-3 times more moderately raining or non-raining low clouds in the EP than in the WP (Kubar and Hartmann 2008). While mean rain rates are similar in the two regions (1.37 mm/hr in the WP versus 1.29 mm/hr in the EP), a higher fraction of rain comes from systems with cloud top below 9.5 km in the EP (47% versus 38%). These differences are not large enough to justify such a stark difference in ω profiles, since a secondary low level peak (weaker than the EP peak) would be expected in the WP as well based on the profiles in Figure 4 of Kubar and Hartmann 2008.

As will be shown, the low-level peak in reanalysis vertical motion persists in the EP regardless of season or ENSO phase. The discrepancy exists even when El Niño convective systems in the EP become very similar to those in the WP (Berg et al. 2002). Stronger surface convergence during El Niño due to southerlies driven by the sea surface temperature (SST) gradient between the equatorial cold tongue and the East Pacific warm pool (Lindzen and Nigam 1987) is likely a cause of convection in the region, rather than a consequence of it (Back and Bretherton 2009). This convergence may be driving some of the bottom-heaviness as well, but given the relaxation of the SST gradient during El Niño, we would expect to see a change in the ω profiles that is not apparent. Additionally, since most reanalyses are forced with similar SST fields, the large variance in the magnitude of the peak ω is puzzling.

An evaluation of reanalysis precipitation data by Pfeifroth et al. (2013) revealed that there is a tendency towards overestimating small to medium rainfall amounts and underestimating heavier rain. While the effects of this could be contributing some to the

bottom-heavy profiles of ω, it is not isolated to the EP region and thus isn't likely to be the main culprit.

Additional studies on precipitation variability in reanalyses reveal that newer products such as the National Aeronautics and Space Administration (NASA) Modern-Era Retrospective Analysis for Research and Applications (MERRA) outperform older ones like the National Centers for Environmental Prediction-National Center for Atmospheric Research (NCEP/NCAR) 40-year Reanalysis Project (NNRP; Kim et al. 2014). The mean state and amplitude of subseasonal variability have also been improved; however, the newer products are still deficient in the probability density of rain intensity. While newer reanalyses have a higher coherence of convectively coupled waves and more realistic MJO propagation when compared with observations, they still anomalously reproduce waves other than the MJO. All reanalyses also typically underestimate high frequency variability on time scales less than three days.

Narrowing down on the EP, the NCEP Climate Forecast System Reanalysis (CFSR) overestimates precipitation and exaggerates variance, even though it performs the best at capturing the diurnal cycle and high-frequency variability (Kim and Alexander 2013). In general, variance is dominated by westward moving disturbances in the region in the annual mean, although these disturbances fade while approaching boreal winter, allowing the variance to become about equal between eastward and westward moving disturbances.

Cumulus convection parameterization schemes are likely responsible for the majority of the disagreement between reanalysis heating products, but cloud radiation

parameterizations, data assimilation schemes, and the large-scale environment are also responsible for a portion (Ling and Zhang 2013). Yokoyama et al. (2014) find that heating in the modern reanalyses (MERRA, the European Centre for Medium-Range Weather Forecasts (ECMWF) Interim Reanalysis (ERAINT), and the Japan Meteorological Agency (JMA) 25-year Reanalysis Project (JRA)) disagree more at upper levels, indicating the importance of radiation. Differences in vertical profiles of latent heating (Yokoyama et al. 2014) versus total diabatic heating (Ling and Zhang 2013) from MERRA lend further support to the importance of the radiative heating and eddy heat flux contributions to Q_1. Most satellite retrievals, on the other hand, undersample shallow precipitation and thus miss some of the low-level heating (Chan and Nigam 2009). At the same time, heating derived from a few of the same reanalyses disagree in both the number and height of the maxima (Ling and Zhang 2013). In one case (MERRA), the heating is shown to have a trimodal structure (see Figure 3, right) but the ω profile is more unimodal or very weakly bimodal (see Figure 1, right). This is because the reanalysis heating derived by Hagos et al. 2010 is likely to be contaminated by diabatic heating not necessarily associated with precipitation such as radiative and eddy sensible heat fluxes.

The accuracy of vertical motion and heating profiles in the EP is important due to their relationship to large-scale circulations such as the Walker and Hadley cells. Many studies state the importance of the large-scale on modulating convection, although it is important to note that many use reanalysis profiles that we are calling into question. Yokoyama and Takayabu (2012) find that shallow convergence (1000-925 hPa) in the

EP is correlated with moderately deep rain from organized systems and shallow rain from congestus, with coefficients of 0.66 and 0.75, respectively. Their conclusion states that the shallow convergence "can primarily be an external forcing to generate shallow rain from congestus", while deeper systems in the EP are driven by synoptic-scale disturbances.

However, causality is uncertain in the literature. There is also evidence that latent heating from deep convective systems is a large portion of the forcing mechanism for these circulations, and so changes in the structure of convection therefore should have an effect on the dynamical response. Schumacher et al. (2004) showed that an increase in the elevation of peak heating leads to an increase in the elevation of the circulation centers in the Walker cell and a strengthening of the large-scale upper level response in an idealized primitive equation model. They also note that regional variations in heating profiles further alter the large-scale atmospheric response.

In addition to the interaction with deep circulations, convection and the resultant heating changes also interact with the SMC that includes return flow near the top of the boundary layer simultaneous with that in the upper troposphere. This circulation has been observed both in situ (Zhang et al. 2004) and in reanalyses (Trenberth et al. 2000; Zhang et al. 2008), but also modeled (Nolan et al. 2007) in the EP.

Some implications for climate sensitivity have been drawn from reanalysis vertical motion profiles in the EP, further stressing the importance of accurate depictions of these profiles. Sherwood et al (2014) created a lower tropospheric mixing index (LTMI), about half of which is made up of the ratio of shallow to deep overturning,

signified by D. The LTMI is correlated well with climate sensitivity in GCM's. Since reanalyses produce such low maximums in vertical motion, they have a higher value of D than nearly all model runs, which the authors use to infer a higher climate sensitivity. However, if the reanalyses are producing large D erroneously, the results of Sherwood et al. (2014) can be questioned.

In the face of the above discrepancies, it is difficult to determine exactly where the diabatic heating peak occurs in reality. Observations tend to point towards a peak in the mid to upper levels of the atmosphere for regions like the ITCZ, but there are still questions left unanswered. Will more sensitive instruments change our view of convection in the tropical eastern Pacific? Or are reanalyses simply misrepresenting convection and the associated atmospheric circulations there? This thesis will investigate precipitation statistics from space-borne radar in the Pacific, to first analyze differences between echo sensed by the TRMM PR and new higher sensitivity GPM DPR in section 3 and then look at differences in EP and WP echo from the TRMM climatology in section 4. Section 5 will compare field campaign datasets to reanalysis fields to help answer these questions and show that EP reanalysis vertical motion profiles are not supported by observations. The majority of literature seems to take reanalysis data as truth in the EP region, but there is evidence to the contrary, at least in regards to vertical profiles of Q_1 and ω.

2. DATA AND METHODS

2.1 Reanalyses

The eight reanalyses chosen for this study include both older and state-of-the-art datasets (Table 2), and will be compared with satellite retrievals to examine the structure and properties of vertical motion and heating profiles in the Pacific. The selected reanalyses are the JRA (Onogi et al. 2007), ERAINT (Dee and Uppala 2009), MERRA (Rienecker et al. 2011), the ECMWF 40-year Reanalysis (ERA40) (Uppala et al. 2005), NNRP (Kalnay et al. 1996), the NCEP-Department of Energy (DOE) Reanalysis Project (NDRP) (Kanamitsu et al. 2002), NCEP CFSR (Saha et al. 2010), and the National Oceanic and Atmospheric Administration-Cooperative Institute for Research in Environmental Sciences (NOAA/CIRES) Twentieth Century Reanalysis Version 2 (20CR) (Compo et al. 2011).

Table 1 – Reanalysis data sets. From Stachnik and Schumacher (2011).

				Analysis Output Resolution		
Dataset	Source	Data Range	Resolution	Horizontal	Pressure	Temporal
JRA	JMA	1979-2007	T106L40	1.125° x 1.125°	23 levels	6-hourly
ERAINT	ECMWF	1989-present	T255L60	1.5° x 1.5°	37 levels	6-hourly
ERA40	ECMWF	1957-2002	T159L60	2.5° x 2.5°	23 levels	6-hourly
NNRP	NCEP/NCAR	1958-present	T62L28	2.5° x 2.5°	17 levels	6-hourly
NDRP	NCEP/DOE	1979-2008	T62L28	2.5° x 2.5°	17 levels	6-hourly
CFSR	NCEP	1979-present	T382L64	0.5° x 0.5°	37 levels	1-hourly
MERRA	NASA	1979-present	$^2/_3$° x $^1/_2$°, L60	$^2/_3$° x $^1/_2$°	42 levels	3-hourly
20CR	NOAA/CIRES	1871-2008	T62L28	2.0° x 2.0°	24 levels	6-hourly

While these datasets differ in their model physics and resolutions, all but the 20CR assimilate surface, upper-air, and satellite observations. The 20CR only ingests surface pressure, SSTs, and sea ice coverage. Although the CFSR is a fully coupled land-ocean-atmosphere reanalysis, the remaining seven datasets are all forced with specified SSTs.

The processing performed on these datasets by Stachnik and Schumacher (2011) is described as follows: relevant varibles were regridded to 2.5˚ x 2.5˚ horizontally using either spherical harmonics or bilinear interpolation. Vertical regridding was also performed for upper air variables into 10 hPa increments from 1000-10 hPa using linear interpolation. Any errors due to the regridding process were corrected by specifying the appropriate bounds for each variable before monthly averages were calculated. The MERRA dataset is available at highest temporal resolution (6-hour), and so this will be used for direct comparison to 6-hourly field campaign soundings.

2.2 Satellites

The TRMM satellite was launched as a joint venture by both NASA and the Japan Aerospace Exploration Agency (JAXA) in November 1997, originally scheduled to perform a three-year mission. In 2001, the satellite was boosted from 350 km altitude to 402.5 km in order to save fuel and extend its lifetime (Shimizu et al 2009). This move proved quite useful, as the TRMM satellite remained in full operation through September 2014. Fuel began to run too low in October 2014, and so instruments were intermittently powered off until the satellite was shut down completely in April 2015.

The three main instruments aboard the satellite were the TMI, the PR, and the visible infrared scanner (VIRS). This study will use only the TRMM PR, a K_u-band radar operating at 13.8 GHz. It was the world's first space-borne radar and now provides a robust, 16-plus-year climatology of three-dimensional precipitation statistics over the tropics and subtropics, with data available from 35˚S-35˚N.

NASA and JAXA launched the successor to TRMM, the Global Precipitation Measurement (GPM) core satellite, in February 2014. It flies at 407 km and takes measurements from 65˚S-65˚N. On board is a dual-frequency PR (DPR), which adds a K_a-band radar at 35.55 GHz with a smaller swath width than the K_u-band (120 km vs 245 km; these widths will be referred to as "inner" swath vs. "full" swath), but the K_a-band has greater sensitivity to better discern shallow and weak rainfall as well as snow at higher latitudes. The K_u-band radar frequency was reduced to 13.6 GHz for GPM, but transmitting power was increased from 500 W to 1000 W to compensate for range loss due to the higher orbit at launch. K_u-band retrievals have a nominal minimum detectable reflectivity threshold of 18 dBZ, while the K_a-band should theoretically reach 12 dBZ at high sensitivity (Hou et al. 2014).

On average, there are about two overpasses of each satellite per day in each of the two selected regions for this study. The orbital periods for TRMM and GPM are 91 and 95 minutes, respectively. Figure 4 depicts reflectivity from selected overpasses of the TRMM (top) and GPM (bottom) satellites over the EP region. Because of the increase in global coverage of GPM, the satellite passes mainly in the north/south direction near the equator, but TRMM cuts out a more northwest to southeast swath.

Thus, each pass of TRMM through the domain covers more area than GPM, and more echo overall can be observed. For most of the overpasses, the entirety of the swath lies within our chosen domains (Figure 4, bottom left), but some swaths are only partially within the region (Figure 4, bottom right).

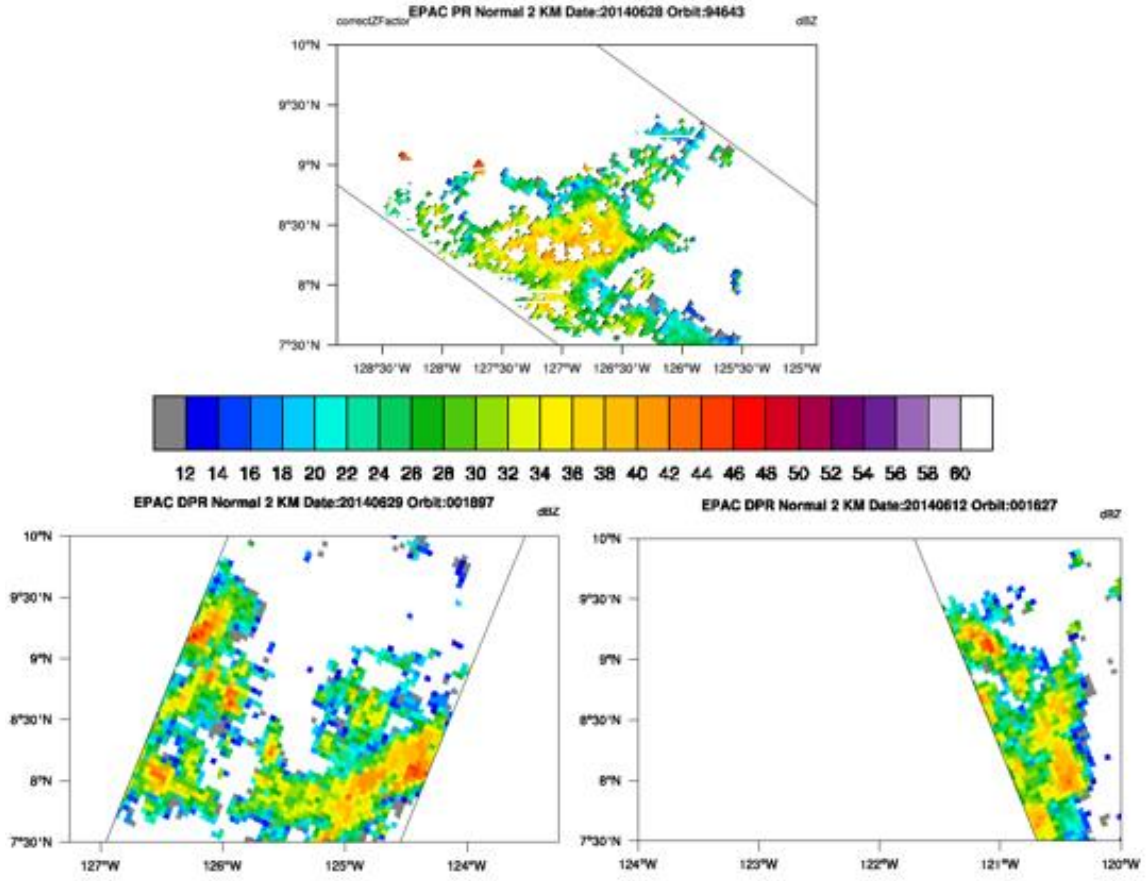

Figure 4 – Filtered reflectivities from TRMM PR (top) and GPM DPR (bottom) over the EP domain. One GPM overpass that passed completely through the domain (bottom left) and one that caught the edge (bottom right) are pictured.

Our processing stream for data from TRMM and GPM includes organizing the data into monthly histograms and saving them in IDL .dat and NETCDF file format for the respective satellites. Each echo-containing pixel is integrated into the histogram based on latitude, longitude, height, reflectivity, storm top height (STH), and precipitation type (stratiform, convective, other, shallow isolated, shallow non-isolated; the latter two will be discussed shortly). Storm top heights are included in the standard products of these satellites and are defined as the altitude of the highest range bin containing precipitation echo above the minimum thresholds, with the caveat that there must be six contiguous bins in order to filter out noise (Toyoshima et al. 2015). The histograms have a final horizontal resolution of 2.5˚ by 2.5˚, with reflectivity binned from 12 to 60 dBZ in increments of 2 dB. Height is binned from 0.5-20 km by 500 m, and STH is binned from 1-20 km by 1 km for the stratiform and convective types. For the shallow types, STH is binned from 0-5 km by 250 m.

Precipitation type partitioning for the TRMM PR is performed by the 2A23 algorithm (Awaka et al. 1997, 2007, 2009). Since stratiform precipitation typically falls from the cold upper atmosphere into warmer air below, ice particles melt after passing the 0˚C isotherm. While melting from the outside in, the hydrometeor forms a liquid film while remaining at a larger size than if it were all liquid, so the radar returns a stronger pulse at that level that manifests as a horizontal bright band. The 2A23 algorithm looks vertically through a column for the bright band to define stratiform precipitation regions. The algorithm also uses a horizontal peakedness separation algorithm to determine convective cores based on Steiner et al. (1995) and produces a final classification by

combining the two analyses. Although algorithm improvements have reduced errors in these separations, some issues are still possible, especially for latent heating calculations (e.g., some echo in tropical cyclones is classified as stratiform, when evaporative cooling is certainly not strong in the moist lower troposphere; Liu et al. 2015). If a pixel cannot be defined as stratiform or convective by one of the two methods, it is assigned the type "other." Echo of this type is typically associated with thick non-raining or lightly raining anvil clouds, and as will be shown later, contributes very little to total rainfall.

The data were further separated to include shallow isolated and shallow non-isolated precipitation types, which have tops reaching no higher than 1.5 km below the climatological 0˚C isotherm (TRMM PR Team, 2011). Any shallow pixel adjacent to a pixel with deep echo is considered non-isolated, and the rest are isolated. Since these systems form via the warm rain process (collision and coalescence), they will be considered convective in nature (Schumacher and Houze 2003b; Funk et al. 2013).

For the DPR, path-integrated attenuation estimates are performed with the dual-frequency algorithm inside the inner swath of the satellites view, but fall back to the K_u-only algorithm for the outer swath or locations within the inner swath where the dual-frequency calculation is unavailable. DPR precipitation type sparations are performed by both by the single-frequency TRMM-era algorithm and a dual-frequency separation algorithm (Le and Chandrasekar 2013). There is also a high sensitivity (HS) dataset using only the K_a data. Five histograms were created in order to determine the differences between the datasets: K_a HS (inner only), DPR-inner, DPR-full, K_u-inner, K_u-full.

The DPR dual-frequency products for April 2014-March 2015 produce stratiform rain fractions that are much higher than we should expect, 47.2% vs 37.7% from the much more established TRMM dataset in the tropical Pacific region analyzed (5˚S-15˚N, 130˚E-90˚W; see section 3). This discrepancy stems at least in part from the rain-type classification, as the DPR dual-frequency dataset has 2.5% more stratiform pixels and 15.4% less convective pixels than the K_u-only. Previous work has found sufficient agreement between the PR and ground-based separations (Schumacher and Houze, 2000; Liau et al. 2001) so the DPR is likely suffering from an algorithm deficiency. Only the K_u rain type will be used in this study.

Since GPM has only been collecting data for a little over a year, there is little analysis in the literature. One paper published shortly after launch (Kubota et al. 2014) evaluated the DPR precipitation algorithms over oceanic regions using synthetic data based on retrievals from the TRMM PR. The authors found that retrievals from only the K_a-band were subject to attenuation and were thus underestimated, but the only K_u-band and DPR (K_u and K_a) algorithm retrievals were accurate. Unexpectedly, the K_u-only data performed better than the dual-frequency retrievals, which the authors attribute in part to their methodology.

A more recent study using actual GPM data from April to August 2014 (Toyoshima et al. 2015) also showed that the K_a retrievals may not add as much new information as originally thought. Their analysis compared STH histograms from K_u-only, K_a matched scan (MS) and K_a HS retrievals, using only near-nadir data to avoid contamination from side-lobe clutter. By comparing STHs generated with different

reflectivity thresholds (8-20 dBZ in 2 dB increments) to those generated by the DPR algorithm, they found that the K_u-only data performs better than expected, with a minimum threshold between 12 and 14 dBZ producing the best results as opposed to the 18 dBZ theoretical threshold. This, in addition to some error in the K_a-band due to the non-Rayleigh scattering effect, leads to a lower than expected improvement in the high-sensitivity data. Section 3.1 will look further into the differences between the regular DPR data and the DPR HS retrievals.

2.3 Field Campaigns

The Pan American Climate Studies (PACS) program ran TEPPS as its first study. It was also the maiden voyage of the NOAA ship R/V *Ronald H. Brown* (hereafter *RHB*). Instruments aboard the *RHB* included rawinsondes launched at ≤4 hr intervals and a C-band Doppler radar, as well as a number of rain gauges and disdrometers for calibration. Yuter and Houze (2000) give an in depth overview of the intertropical convergence zone (ITCZ) portion of the cruise, which took place from 8 t 23 August 1997 at 7.8ºN, 125ºW, and describe the full suite of meteorological and oceanographic instruments on board.

Only one other major field campaign with surface-based observations has occurred in the tropical EP. EPIC took place in September and October of 2001, with much more in-depth data collection than for TEPPS due to the addition of a second ship as well as two aircraft. The *RHB* was stationed near 10ºN, 95ºW, with a vertically pointing, K_a-band cloud radar aboard for this mission. The aircraft were equipped with

precipitation radars, but also collected in situ wind and thermodynamic data and released dropsondes and ocean probes over a 4º by 4º network surrounding the station site (Raymond et al. 2004).

Similar campaigns have taken place in other regions of the Pacific, including KWAJEX in the west-central Pacific (8.7 ºN, 167.7ºE; Yuter et al. 2005) and TOGA-COARE in the WP (2°S, 156°E; Webster and Lukas 1992). We will use radar and sounding data collected in these campaigns later in Section 5 to show the robustness of relationships between rainfall statistics and heating and vertical motion, regardless of the region of interest.

Profiles of kinematic variables provide an important look into air motions around and within precipitation systems. In order to accurately determine these values over the large domains of the various field campaigns, a network of multiple sounding measurements are required in the region surrounding the radar site. Zhang and Lin (1997) developed the technique of variational objective analysis (VOA), which makes adjustments to the sonde data with ancillary observations such as radar-derived surface rain and top-of-atmosphere surface fluxes within their model uncertainty bounds to fit conservation laws. Previous methods only considered mass conservation, while VOA conserves column-integrated mass, moisture, static energy, and momentum. This method reduces error in vertical velocity measurements, especially during disturbed periods (Waliser et al. 2002). In addition, it allows for higher accuracy at larger temporal scales, and so 6-hourly or better averaged field campaign data will be used.

Since radiosondes have poor spatial and temporal resolution, Mapes and Lin (2005) created a simple analysis method to derive zonal and meridional winds and divergence profiles for single Doppler radar datasets such as those from the *RHB*. They organized hourly radar data into a cylindrical 24 x 12 x 36 grid with cells of 15º x 8 km x 500 m. After the radial velocities are dealiased using a histogram method, they are fed into a velocity-azimuth display (VAD) analysis, creating hourly wind and divergence profiles for circles of different radii centered on the radar. This method requires adequate echo coverage since radial velocities cannot be measured in the absence of hydrometeors, and so the raw data are re-binned into larger spatial sections in preparation for the analysis to increase the amount of echo, especially in the upper levels.

There are a few small errors associated with this method, including a particle fall speed overestimation near the melting level that is apparent in the time-mean divergence profiles, as well as a systematic increase in upper level divergence with decreasing radius. Despite this, the data are sufficient for comparative study. A linear regression of the VAD divergence from a number of field studies calculated against reflectivity estimated rainfall (Mapes and Lin 2005) showed that the dominant pattern in these systems includes a period of low level convergence and convective rain, evolving over several hours into stratiform rain with mid-level convergence as expected.

3. TRMM AND GPM OVER THE PACIFIC

The long length of the TRMM PR dataset makes it ideal for climatological study. Before using data from the PR to make inferences over the EP and WP (solid boxes in Figure 5), this thesis compares PR products with GPM products over a larger domain encompassing much of the tropical Pacific (dashed box in Figure 5). The larger domain increases the size of the dataset to avoid any sampling errors arising from the non-simultaneity of the satellites orbits. With a full year of GPM data over this large region, any variation on diurnal timescales would be sufficiently averaged out.

In order to include the ITCZ, the WP warm pool, and at least a portion of the EP cold tongue while remaining primarily over oceanic regions, the chosen domain covers the tropical Pacific from 5˚S-15˚N and 130˚E-90˚W. Yearly averaged total rain and stratiform rain fractions from the TRMM PR are also depicted here.

The ITCZ is clearly defined in Figure 5 (top) but has a rainfall minimum in the central Pacific. Also clear are the WP warm pool and south Pacific convergence zone (SPCZ), and there is a faint hint of a double ITCZ feature centered near 5˚S in the EP. The climatological stratiform rain fraction is noticeably higher in the EP region than the WP (Fig. 5, bottom), which should increase heating at upper levels in comparison to regions of similar rainfall amounts in the WP following Schumacher et al. (2004).

No comparisons have been published between the PR and DPR at this time, and there is still very little in the literature using post-launch GPM data. Although earlier studies have praised the K_u retrievals from the new DPR algorithm (Kubota et al. 2014) and found that improvements in the HS K_a retrievals were less than expected

(Toyoshima et al. 2015), the analysis thus far has been rather lacking. Storm statistics will first be compared between the K_u-inner and HS datasets in section 3.1. Then in section 3.2 the differences in GPM K_u-full and PR statistics will in turn justify the use of the PR for regional comparisons.

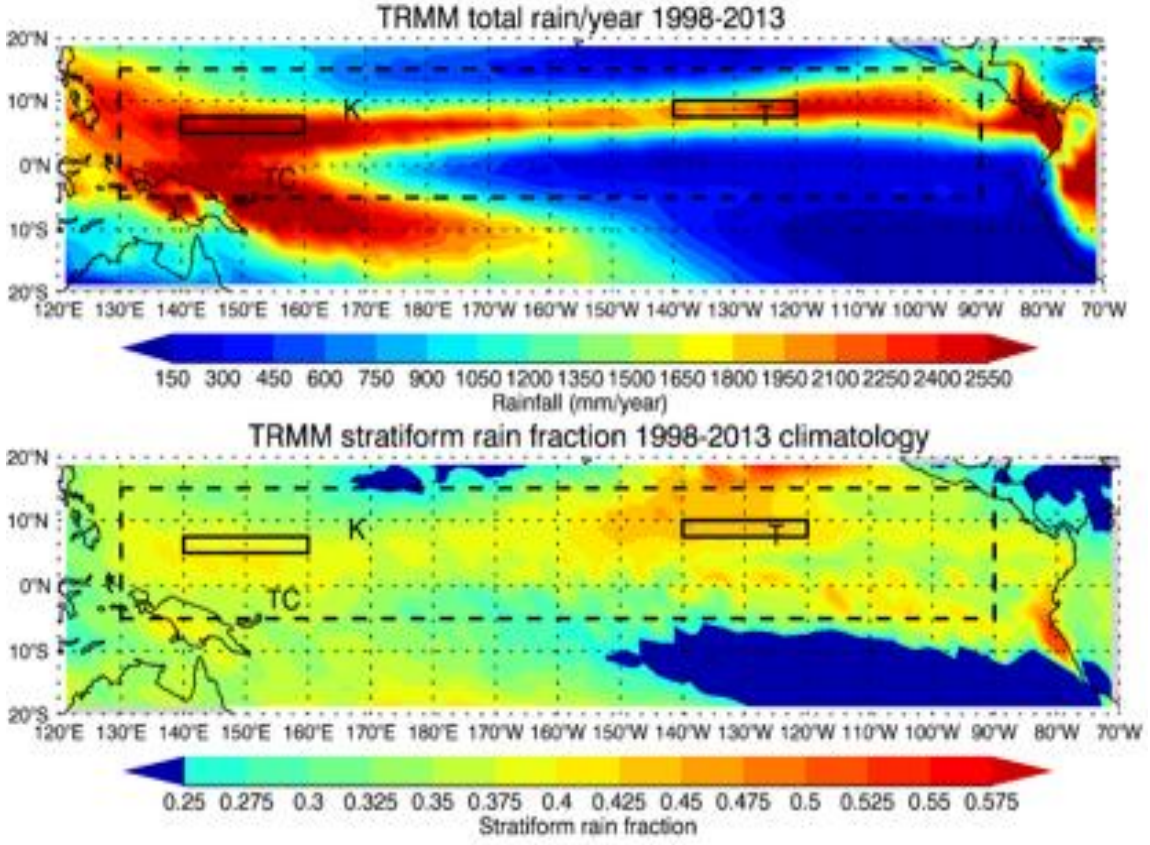

Figure 5 – Climatology of TRMM rainfall (top) and stratiform rain fraction (bottom) for 1998-2013. The dashed box represents the region used for TRMM-GPM comparisons. The two smaller boxes are the WP and EP regions to be used later. The T represents the location of the TEPPS field campaign, TC of TOGA-COARE, and K of KWAJEX.

3.1 GPM K_u-inner and HS Comparisons

Higher radar sensitivity should allow for better sampling of weaker reflectivity areas at the top of a cloud, which would manifest as an increase in STH relative to the K_u data. Figure 6 shows the GPM HS (red) and K_u-inner (blue) STH histograms plotted as a line graph, separated into the five precipitation types defined in section 2.2. At all heights, fewer deep convective pixels (dotted lines) are observed by the high sensitivity dataset, which is related to the misclassification problems discussed in section 2.2. But the HS convective histogram peaks at 8 km, while the K_u peaks at 5-6 km. Stratiform pixels (solid lines) comprise the majority of all rain types, and they are observed more in the HS retrievals above about 10 km as expected.

The shallow categories (i.e., non-isolated and isolated combined) make up 11.9% and 8.7% of the total pixels for the K_u-only and HS retrievals, respectively, though it is unclear here whether the HS is missing shallow echo or elevating echo into the deep types. The other category is the smallest portion of the data. Since it is primarily non-raining echo with very low reflectivity, it provides a negligible amount of latent heating.

These histograms do not give any information on the reflectivity and profile shape of the cloud and precipitation systems, just their distribution of storm height. Visualizing storm statistics over large time and space scales and for all vertical levels can be more effectively accomplished by contoured frequency by altitude diagrams (CFADs; Yuter and Houze, 1995). CFADs were originally developed to examine ensemble properties of the convective life cycle, but are also effective for climatological studies. CFADs by definition have height as the y-axis, and the x-axis is the value of the

parameter being plotted, typically reflectivity or vertical velocity. The contours are frequency of occurrence. Historically, the contours are normalized by height, meaning that the sum of values at one vertical level within a CFAD is unity.

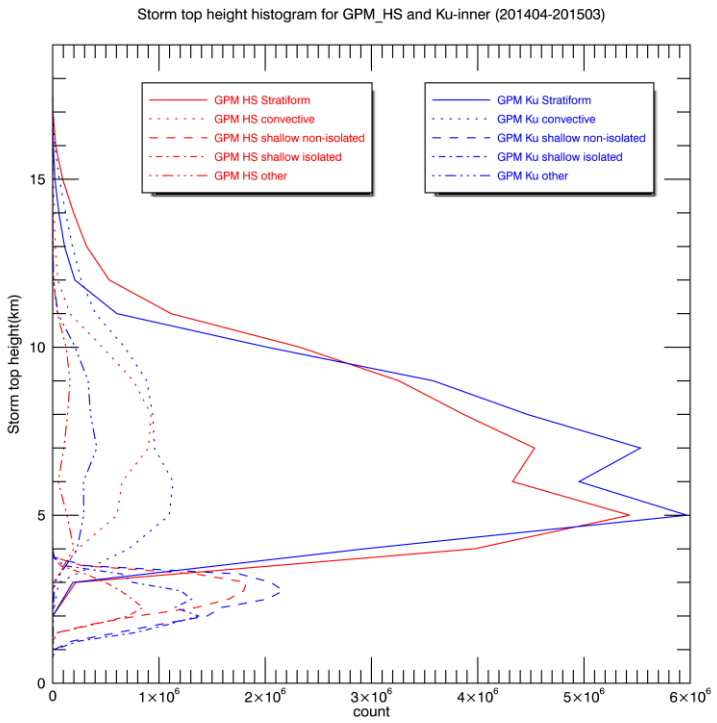

Figure 6 – Histogram of storm top height pixel counts from the GPM HS (red) and K_u-inner (blue) for the period April 2014-March 2015. Data has been separated into the five types (convective, stratiform, shallow isolated, shallow non-isolated, and other).

In order to gain more information about storm type classification, CFADs in this study will also be normalized by the total number of echo-containing pixels for the satellite in its time period and region of interest. In other words, the sum of values for every point in all five CFADs in column 1 or 2 is unity, and in column 3 is zero. Figure 7 includes these CFADs for the K_a HS data (column 1), the corresponding inner swath of

the K_u DPR data (column 2), and the difference between them (column 3) from April 2014-March 2015, where each row represents one of the five precipitation types.

The HS identifies more overall stratiform echo and less convective echo relative to the K_u, in agreement with the STH histograms (though this is harder to see in the stratiform STHs than the CFAD). In the individual plots for these deep storm types, the "warmer" red colors are indicative of this. The positive HS-K_u differences generally occupy the space between 10 and 20 dBZ where HS should be more sensitive, although there is some additional HS echo observed below 5 km and greater than 20 dBZ in the stratiform difference CFAD. This is likely due to attenuation (i.e., the negative difference values below 5 km and at high reflectivities are when the HS signal becomes fully attenuated, thus shifting more relative occurrence to lower reflectivities).

Attenuation is more of an issue in convective rain. The convective difference CFAD has a broad negative region at low levels between about 25 and 42 dBZ, with the maximum centered between 36 and 39 dBZ. A thinner line of negative values stretches towards lower reflectivities and higher altitudes; this feature is seen in the stratiform difference CFAD as well. This strong attenuation renders the HS dataset unusable for examining the hypothesis of this study, but it is still valuable as a point of comparison to see that the K_u doesn't miss enough echo to drastically effect heating profiles.

The shallow types occur less frequently in the HS dataset, although the difference CFADs show a narrow band of increased near-surface reflectivity as well as enhanced HS occurrence above 3 km at weak reflectivities. The method of normalization employed here only allows us to see frequencies relative to the other storm types.

Normalizing by each storm type individually will make it easier to see vertical shifts in their distributions. The plots for this method were almost identical to Figure 7 for all but the shallow storm differences, shown in Figure 8. In both shallow rain types, a positive anomaly stretches from 4 km and 12 dBZ down to the surface at 20-23 dBZ, with negative anomalies in the bottom left corner of the CFAD. We can infer from this that the HS shallow data is increased in elevation relative to the K_u. Some echo classified as shallow by the K_u-only is classified as deep by the HS. Another negative difference sits near the surface at 25-30 dBZ, which is indicative of attenuation in the HS data. Assuming the HS data is more accurate when it isn't attenuating, K_u-only retrievals are missing some echo from upper level, weak reflectivity cloud. In total, HS retrievals see 5% more echo below 20 dBZ than the K_u. HS also elevates some shallow echo, reclassifying it into the deep types due to the STH increase. Estimates of latent heating from K_u-only retrievals are thus likely biased too low in the upper atmosphere, although the absolute magnitude of heating is typically low at these altitudes.

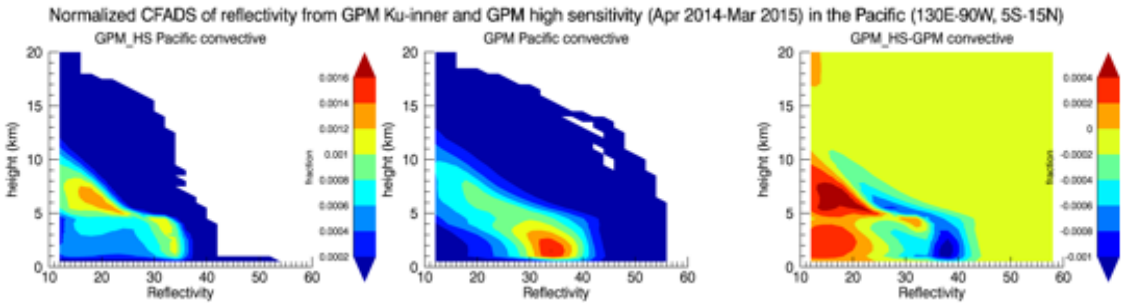

Figure 7 – Normalized Contoured Frequency by Altitude Diagrams (CFADs) of reflectivity over the tropical Pacific (5˚S-15˚N, 130˚E-90˚W) from the GPM HS (column 1) and the inner swath of the GPM K_u (column 2) from Apr 2014-Mar 2015. Column 3 is the difference between them. Data are separated by precipitation type as in Figure 6.

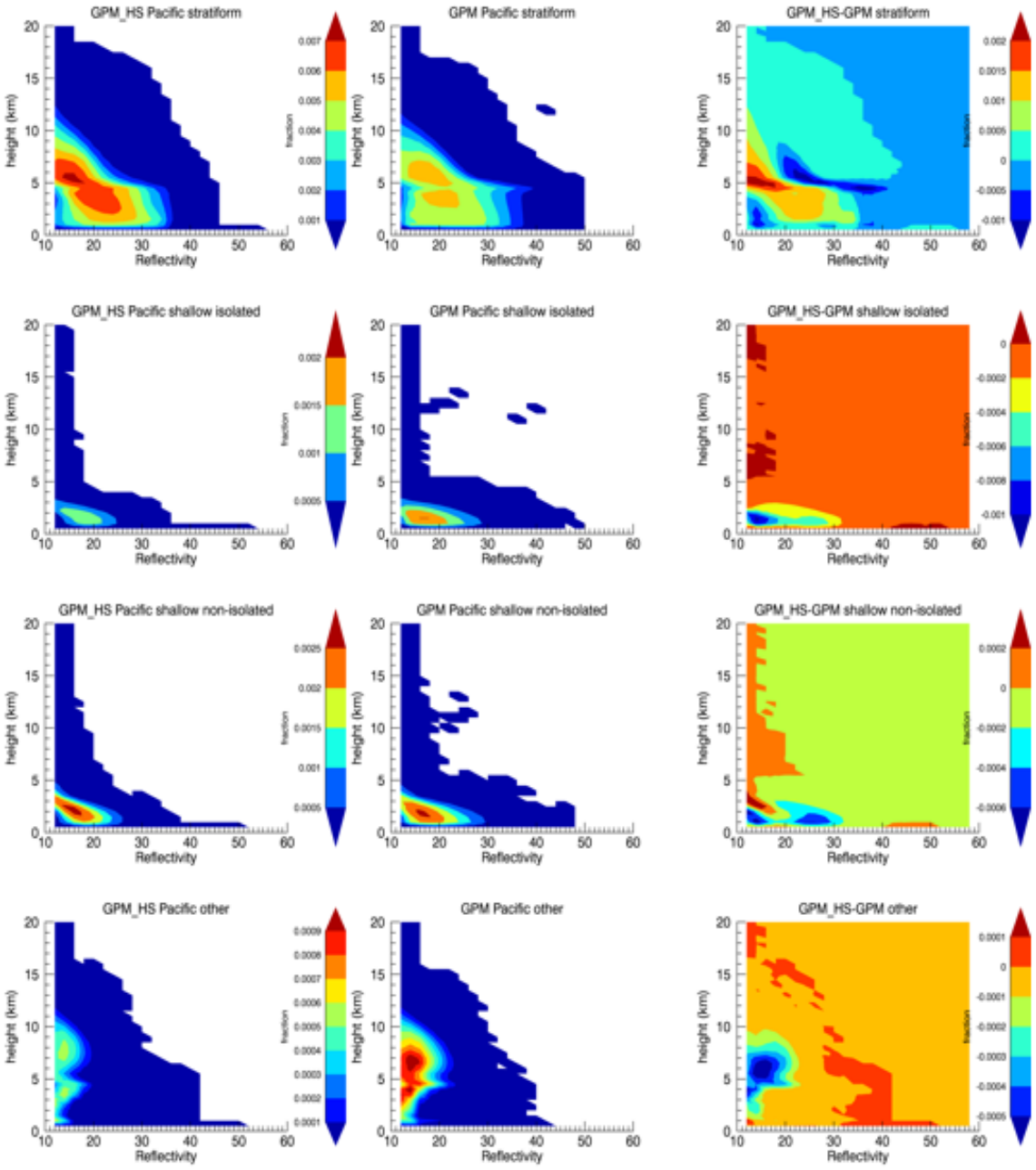

Figure 7 – Continued

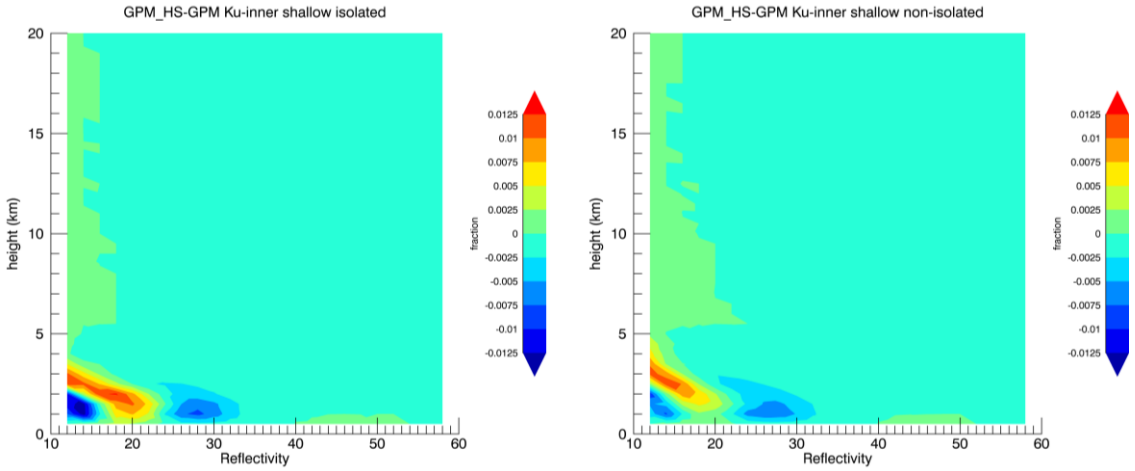

Figure 8 – GPM HS minus K_u-inner reflectivity difference CFADs normalized by storm type for shallow isolated (left) and shallow non-isolated (right) types only.

3.2 GPM DPR and TRMM PR Comparisons

There are known biases in the TRMM precipitation observations away from nadir, with surface rainfall errors of 2.7% over ocean regions pre-boost and -3.2% post-boost (Hirose et al. 2012). These are relatively small errors, and since GPM operates at a similar altitude with a similar swath width to the post-boost TRMM PR, the off-nadir error for GPM precipitation retrievals should be similarly small. A look at the normalized CFADS of the inner and full swaths (Figure 9) for all storm types combined shows that the inner swath observes more echo closer to the surface while the full swath observes relatively more echo aloft, especially at weak reflectivities. Sampling of low level features is more difficult away from nadir due to the parabolic nature of the area cut out by the swath. The full swath observes 4.5% less overall echo below 20 dBZ due to the higher magnitude of the low level differences. At 2 km, where precipitation is calculated in this work, the differences are moderately negative at weak reflectivities and

become smaller in magnitude with increasing reflectivity, so rainfall should be biased slightly negative, in agreement with Hirose et al. (2012).

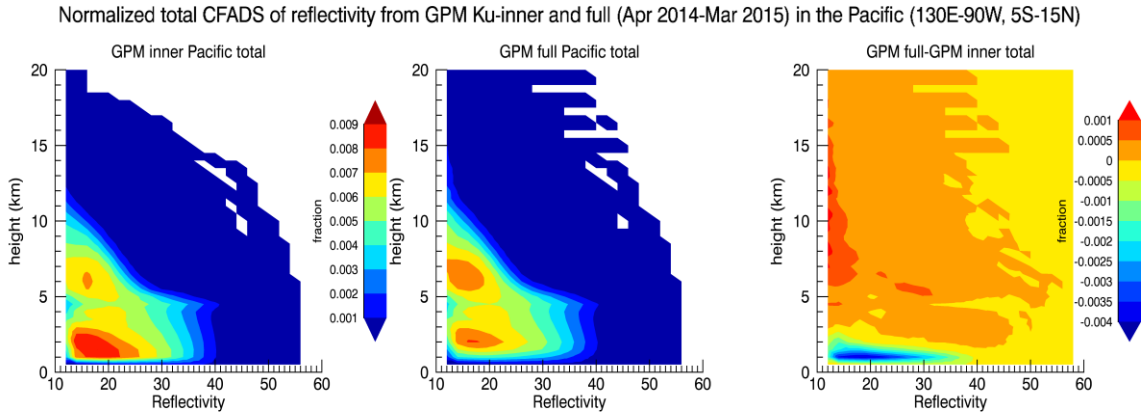

Figure 9 – GPM K_u inner (left) and full (middle) swath reflectivity CFADs and the difference between them (right) for all storm types combined.

Given the lack of improvements using the K_a-band data and the similar errors off-nadir between both satellites, we will compare the TRMM retrievals to those from GPM over the full K_u swath. Statistics were computed for a direct comparison of the six months during which both satellites were in full operation (April-September 2014). A climatological comparison was also made using April 2014-March 2015 GPM DPR data versus yearly averaged TRMM PR data for April 1998-March 2014. Results from these analyses were similar to each other; only the climatological comparisons will be shown here.

It is worth noting that conditions in the Pacific at the beginning of the GPM data collection period were ENSO neutral, but quickly became positive during the boreal spring, maximizing in June 2014 with a NINO3 SST index of around 1 ˚C. The index

declined back to 0.4-0.5 ˚C in the early fall, then rose and fell once more, reaching a minimum in February 2015 near the end of our study period. Although the entire year had positive ENSO indices, an official El Niño was never declared and wouldn't arrive until later in the spring of 2015. Since the domain of interest in this section covers the entire Pacific, these comparisons should be mostly unaffected by ENSO phase.

Figure 10 shows CFADs of reflectivity from both the TRMM PR (column 1), the GPM K_u-full (column 2) and the differences between them (column 3), again normalized by the total of all raining pixels for each satellite. The GPM CFADs on the whole are shifted towards lower reflectivity, but since an appreciable portion of the observed echo is below 16 dBZ which TRMM cannot "see", the distribution is more spread out. This leads to a large area of positive (TRMM-GPM > 0) differences in the CFADs across the majority of the reflectivity spectrum, seen in the third column. GPM observes more echo at very low reflectivity (19.3% more echo below 20 dBZ than the TRMM PR; a much larger improvement than the HS dataset offered over the DPR K_u-only), but also at near-surface altitudes for most observed reflectivities compared to the PR. This is especially noticeable between 30 and 40 dBZ in the convective difference CFAD (top right). The shallow and other precipitation types increase in relative frequency slightly, but the TRMM distribution is shifted towards higher reflectivities once again. The magnitude of the differences is relatively small for the deep types, but are more appreciable in the shallow types in comparison to the magnitudes from each satellite individually.

More information can be gleaned if we return to the traditional normalization-by-height method. In this method, the sum across a single altitude for a single storm type is

unity. At high altitudes, echo is mainly low reflectivity, so a narrow band of higher frequencies is expected, but the high reflectivity echo is of greater interest. In Figure 11, these CFADs are shown for the convective and stratiform types. The shallow and other types do not provide any additional insight and so they are not included here. In this figure, if a particular altitude contains less than 1.5% of the total data for that storm type, it is ignored. For GPM, this includes anything above 10.5 km, but for TRMM it includes anything between 1 and 2 km and above 9.5 km, verifying that TRMM has trouble seeing low-reflectivity, high-altitude echo and higher reflectivity, near-surface echo compared to GPM.

In the region between 2 and 9.5 km, the shift towards lower reflectivities in the GPM dataset is evident, but it less pronounced at lower elevations. The largest differences in the CFADs are aloft where there is less data, and at weak reflectivity (i.e., <20 dBZ) where latent heating is least affected. In the region from 2-5 km where the majority of echo is, the differences are near-zero for convective echo and small in the stratiform type, ranging from -0.04 at reflectivity <20 dBZ to 0.03 at 25-30 dBZ.

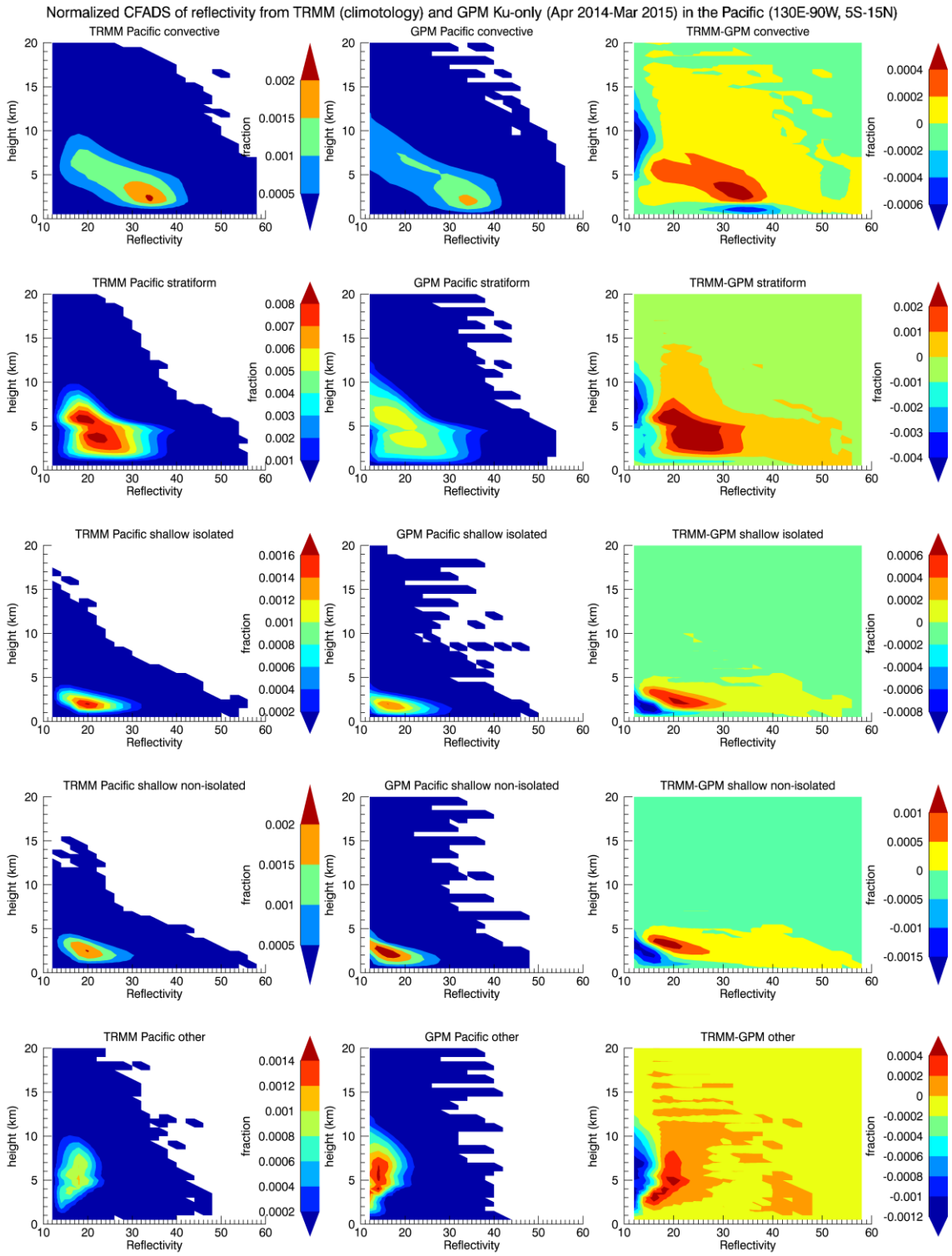

Figure 10 – Same as Figure 6, but the GPM HS data has been replaced by the April '98 to March '14 annual average TRMM climatology, and the K_u-inner data by K_u-full.

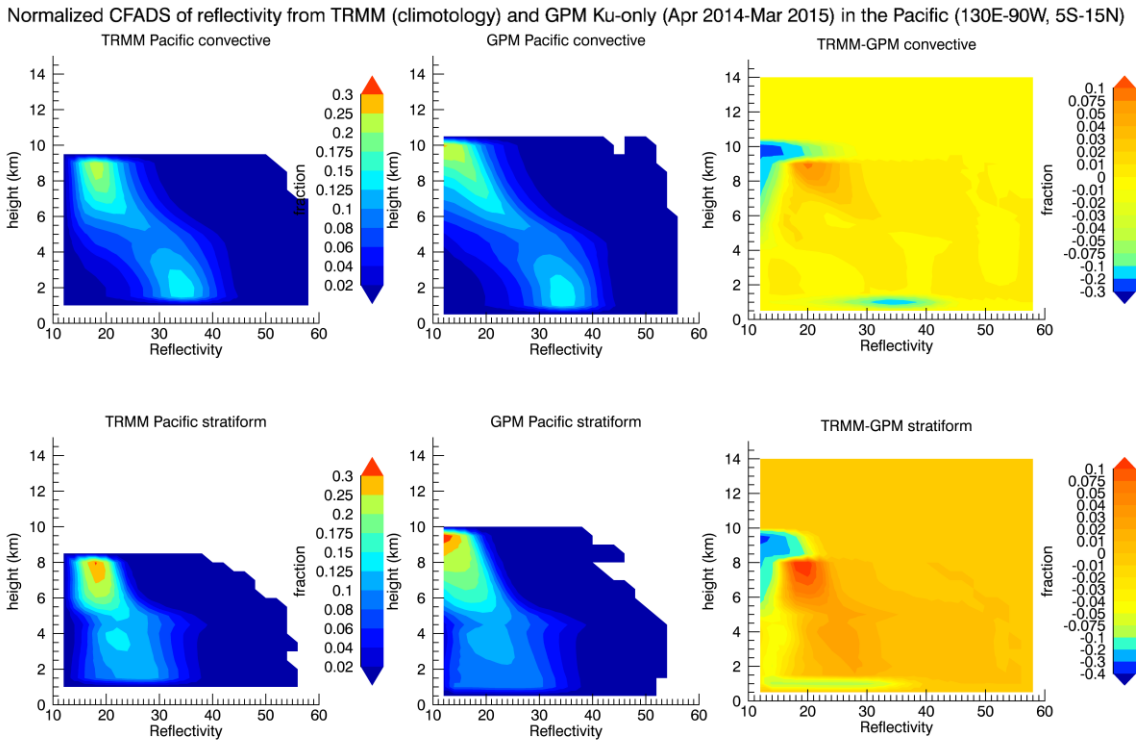

Figure 11 – CFADs normalized traditionally (by altitude) from TRMM and GPM for the stratiform and convective storm types only.

As evidenced above, the lower minimum detectability threshold of the GPM allows for better sampling of lower reflectivity areas at the top of a cloud. A noticeable increase in STH relative to TRMM is expected. Figure 12 (left panel) shows the TRMM climatological average (red) and GPM one-year (blue) STH histograms plotted as a line graph, separated again into the five precipitation types. Stratiform pixels (solid lines) comprise the majority of all observed echo, and there is a double-peak structure in the GPM data at 5 and 7 km. The TRMM PR has only the 5 km peak, but sees many more pixels with cloud tops below 7 km than GPM. Above 7 km the GPM detects more cloud. This pattern is seen in both stratiform and convective clouds, although TRMM sees more

convective activity (dotted lines) up to 8 km. As in the bottom row of Figure 10, GPM shows an increase in the occurrence of anvil cloud (dash-triple dot lines) relative to TRMM. For shallow non-isolated echo, it appears that GPM increases the magnitude, but lowers the altitude of the peak by 250 m. Shallow isolated types have similar magnitudes, but a lower peak in the PR retrievals. Nonetheless, the number count for the shallow categories is small compared to the deep rain types.

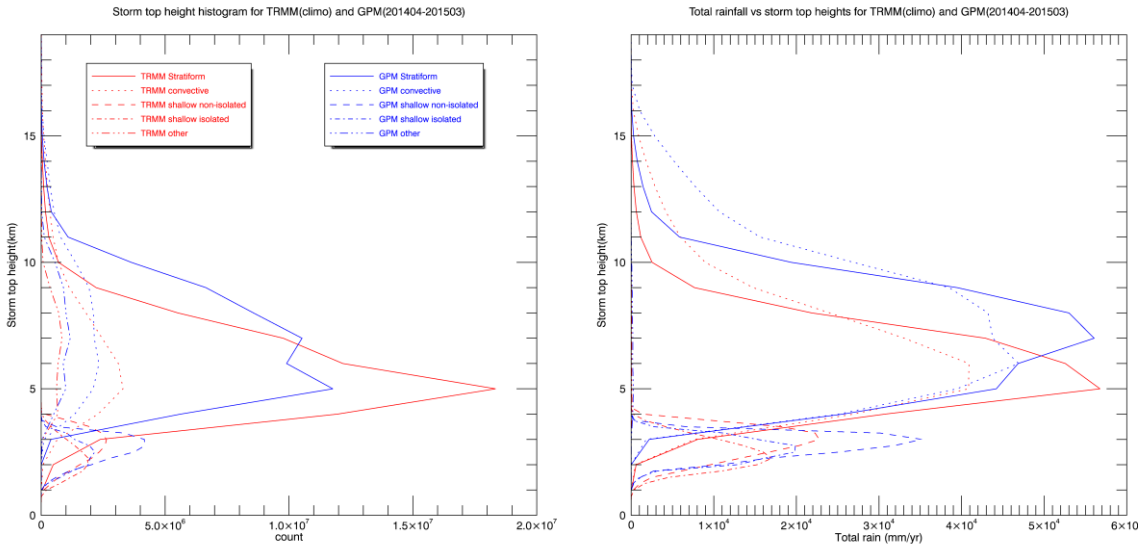

Figure 12 – Storm top height pixel counts from the TRMM PR 1998-2013 climatology (red) and GPM K_u-full April 2014-March 2015 (blue) (left). Contribution of rainfall from different storm top heights for both satellites (right), separated by storm type. Same domain and time period as Figure 5.

Storm top height alone doesn't give full insight into the latent heating produced by these cloud systems. Since latent heating is a direct result of phase changes of water, it correlates well with rain rates. Hence, the right panel of Figure 12 organizes the

TRMM and GPM STH retrievals by total rainfall amount (measured at 2 km to avoid ground clutter) to get a better idea of the latent heating contributions from each precipitation type. The same separation algorithm was used for both satellites, and the TRMM Version 7 (V7) initial convective and stratiform Z-R relations were applied to both TRMM and GPM. The "other" lines are barely visible on the far left, showing that anvil cloud is contributing a negligible amount to the total latent heating, so this type will be ignored throughout the remainder of this thesis.

Convective storms contribute a much larger percentage towards the total rainfall than the pixel counts because of their high rain rates, and since the shallow types are convective in nature, less than half of the rainfall comes from stratiform clouds. Indeed, stratiform rain fractions were calculated from GPM and PR retrievals to be 39.3% and 37.7%, respectively. For the direct comparison of April-September 2014 data, these values are 39.4% for the DPR and 39.8% for the PR. Calculations of stratiform rain fractions across the tropics (20˚S-20˚N) from TRMM PR V5 data were 40% (Schumacher and Houze 2003a) and 38% in the V7 dataset (Funk et al. 2013) so this region and the GPM K_u-band retrievals are consistent with past studies.

It is also apparent that the GPM STHs are 2 km higher at similar rainfall amounts for both stratiform and convective precipitation. The higher stratiform rain fractions and storm top heights both point towards higher heating peaks from GPM compared to TRMM. Shallow storm types have a distribution that is narrower in the vertical from GPM than TRMM, indicating that the increase in STH seen by GPM is elevating some echo into the deeper types. There is a more noticeable increase in altitude in the peak of

the isolated type than the non-isolated. Shallow precipitation types also contribute more towards the total in the right panel of Figure 12 than the left, but this is still only a small fraction of the total precipitation (and thus latent heating) provided by the deeper rain types. Combined, shallow isolated and non-isolated rain types make up 10.3% of the total rain seen by TRMM and 8.7% for GPM. The TRMM values are likely larger due to the shift in the distribution of the shallow types towards higher reflectivities (Fig. 10). Given the similarity in their properties and low overall rain contribution, further analysis in this thesis will combine shallow non-isolated and shallow isolated rain into one shallow storm type.

The overarching hypothesis of this thesis is to show that satellite observations refute the low-level peak seen in reanalysis profiles of vertical motion in the EP. The data from the newer, more sensitive GPM show some additional echo at low levels, but they also have a smaller contribution of shallow rain than the TRMM retrievals. These differences are seen across the Pacific Ocean, and affect both the EP and WP regions. Storm top heights and stratiform rain fractions from GPM point towards a heating peak higher in the atmosphere relative to TRMM, so if we use the TRMM climatology to refute the reanalyses in the EP, GPM would only further corroborate our findings.

The TRMM yearly rainfall of Figure 5 has been broken up by season in Figure 13. The ITCZ shifts south of our regions of interest during northern hemisphere winter and spring, and in fall the WP warm pool produces comparatively less rain than the EP. Both regions produce similar rainfall amounts in boreal summer, and the most rain is produced in this season overall. The majority of the annual zonally averaged latent

heating at this latitude occurs during boreal summer as well (Liu et al. 2015). The JJA and SON rain maps looks most similar to the full year (cf. Figs 5 and 13), but the shapes of the STH plots for JJA (Figure 14) are most similar to the annual ones, with magnitudes near 1/3 of the annual total. Additionally, the JJA CFADs (not shown) do not differ much from the full year. We can infer from this that analyzing just the JJA data will be a large enough sample size and sufficiently representative of the Pacific ITCZ climatologically.

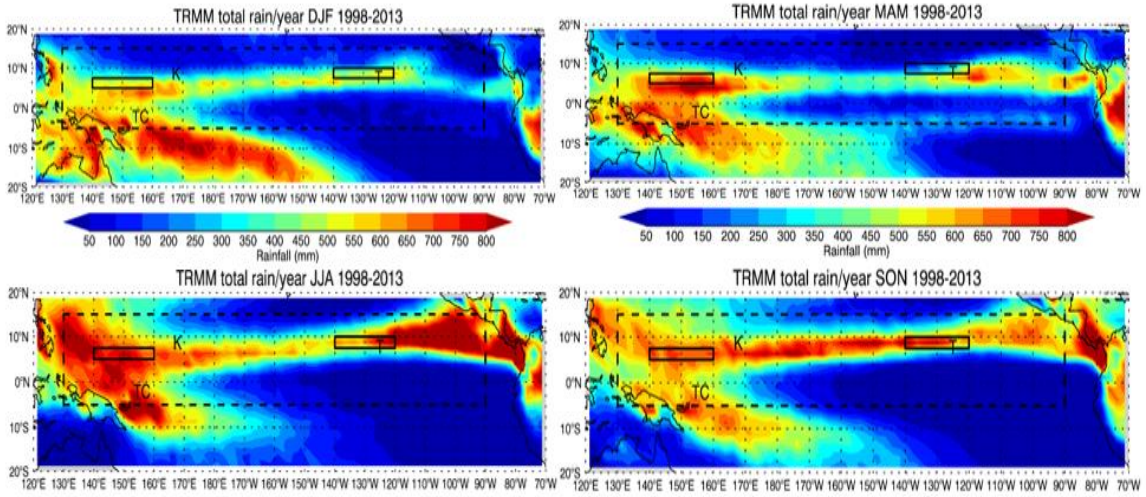

Figure 13 – Seasonal breakdowns of rain across the Pacific as seen by TRMM. Boreal winter (top left), spring (top right), summer (bottom left) and fall (bottom right) are pictured.

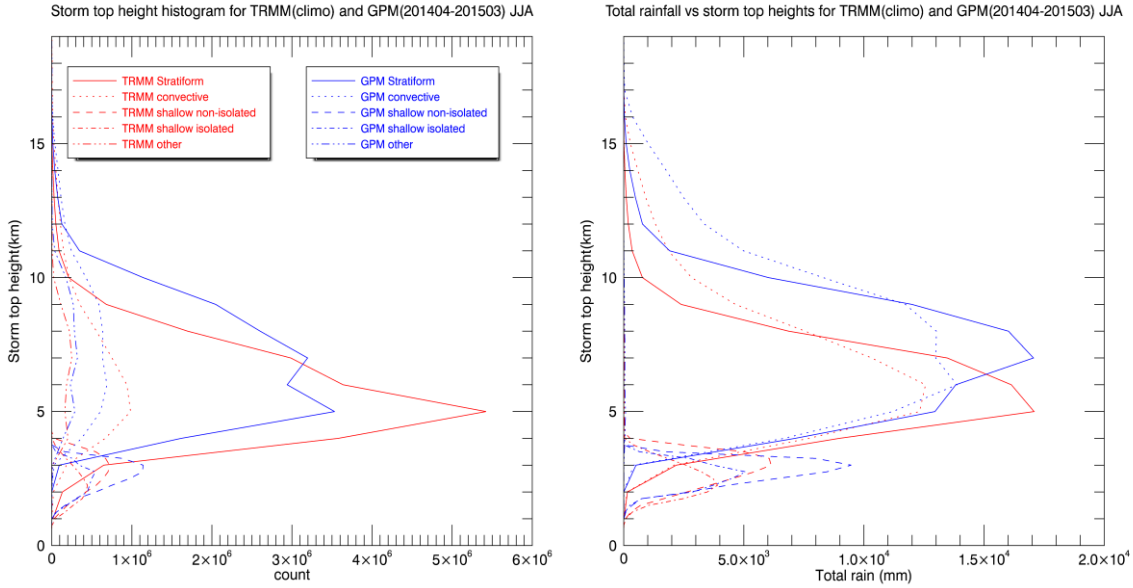

Figure 14 – Same as Figure 12, but for JJA only, and with the TRMM climatology extended to include 2014.

4. EAST AND WEST PACIFIC STORM STATISTICS FROM SATELLITES

Previous work has already established key differences in the characteristics of EP and WP storms. Systems in the EP are shallower than those in the WP, while deeper and larger systems contribute considerably more rainfall (Short and Nakamura 2000, Berg et al. 2002, Cifelli et al. 2007). In order to determine the effects of this on total rainfall differences between the regions, Kubar and Hartmann (2008) compared cloud top probability density functions from CloudSat to rain rates from the Advanced Microwave Scanning Radiometer aboard the Aqua satellite. They demonstrated that mean rain rates were very similar (1.37 mm/hr in the WP versus 1.29 mm/hr in the EP), but a higher fraction comes from shallow systems (defined with tops below 9.5 km) in the EP (47% versus 38%). The reflectivity threshold of CloudSat is -32 dBZ, so cloud tops are much higher than the PR or DPR. The fractions of rain from storms with observable tops below 9.5 km are 98.6% and 97.4% when calculated from TRMM and 86.2% versus 81.5% from GPM. The upper level portion of the storm missed by TRMM and GPM is contributing to the latent heating, but the magnitude is small compared to microphysical processes lower in the troposphere.

Figure 15 includes the EP and WP CFADs from the PR and the difference between them for convective, stratiform, and shallow precipitation types. In terms of volumetric occurrence, 36.4% more shallow reflectivity occurs in the EP, while deep convective reflectivity counts are 52% less. Stratiform reflectivity counts are only 14.9% less in the EP. These differences are significant, but are not nearly as drastic as the

differences in reanalysis ω profiles, which are about three times greater in the WP at 400 hPa and twice as small in the WP at 850 hPa.

There is a small increase in deep convective echo near the surface in the EP and while shallow convection is less common over the WP, it is stronger when it occurs. This is indicated by weakly positive WP-EP differences at higher reflectivities. Above the stratiform bright band in the WP, an increase in echo is seen that can be attributed at least in part to larger aggregates. In the EP below 5 km, the stratiform contours increase in reflectivity as they approach the surface, leading to higher reflectivity values at 2 km, the height where rainfall is calculated. An increase in reflectivity toward the surface occurs when hydrometeors fall through lower level clouds (Hirose and Nakamura 2004; Liu and Zipser 2013). Raindrops falling faster than the speed of the updraft and high humidity at low levels favor this, and these both occur frequently over the ocean. Stratiform cloud base is typically near the 0ºC level so this feature in the EP stratiform CFAD suggests that some convection (likely aged) is being included in the stratiform classification. Vertical cross-sections of various broad stratiform regions (BSRs) are shown from multiple regions in Houze et al. (in press). Reflectivity patterns at times closely resemble numerous small convective cells embedded within the BSR rather than a traditional MCS, but they are still classified as stratiform echo. According to Houze et al., in the WP warm pool during JJA, this type of stratiform precipitation occurs just 12.5% of the time, while it occurs 49% of the time in the EP. Figure 15 shows that the WP stratiform rain also has the most robust reflectivities at all heights, likely due to the overall stronger deep convection, which ultimately feeds the stratiform rain regions.

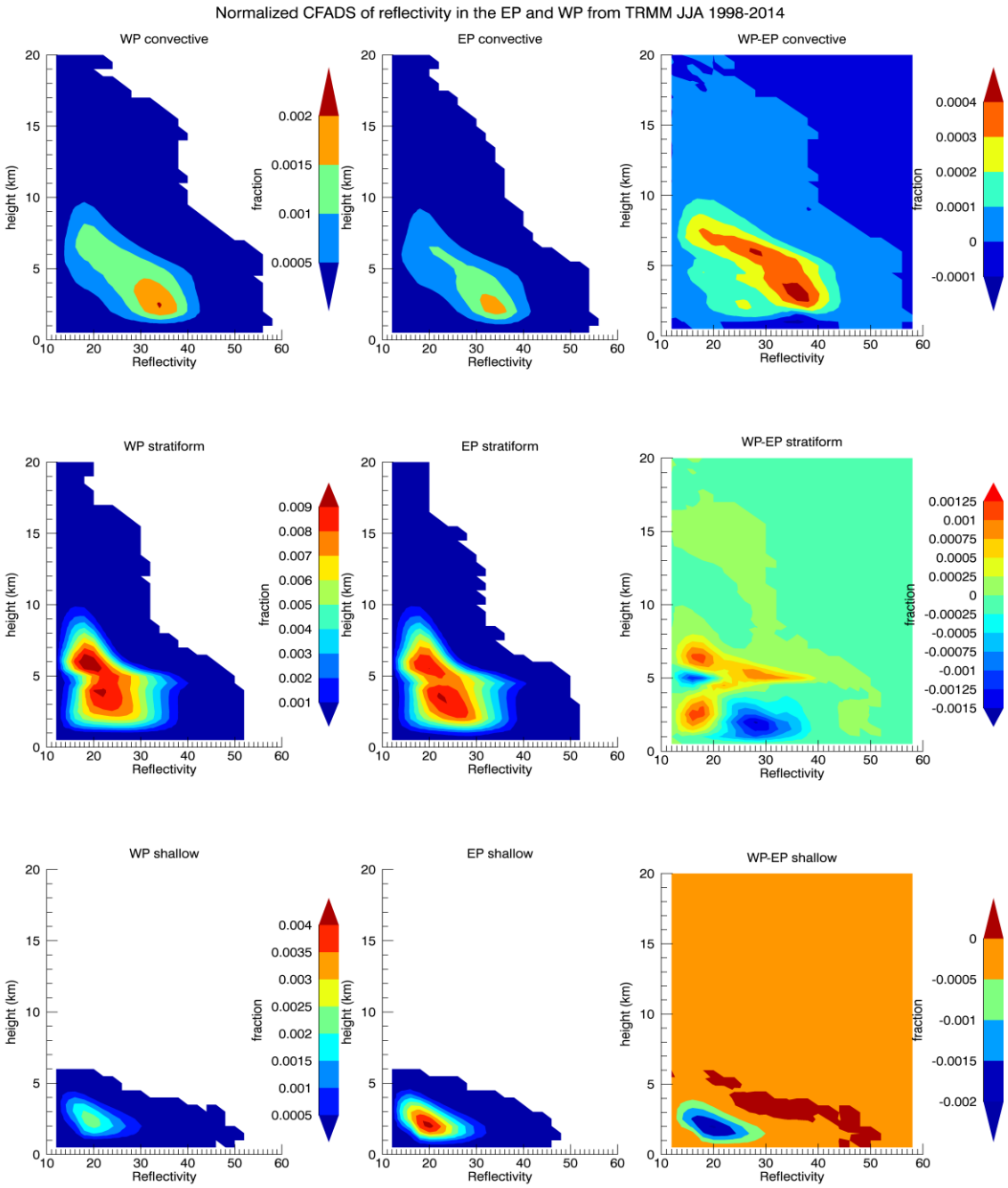

Figure 15 – Normalized CFADs of reflectivity from TRMM PR over the WP (left column) and EP (middle column) regions, as well as the difference between them (right column). Convective (top row) and stratiform (middle row) precipitation types remain unchanged, but the shallow isolated and shallow non-isolated have been combined into one shallow type (bottom row).

.

Figure 16 (left panel) shows that the WP has more convective pixels with slightly higher STHs (~1 km) compared to the EP. Shallow rain types are more common in the EP with a peak in the distribution about 500 m lower. The rain contributions from the shallow types have similar shapes, but the magnitudes are a larger proportion of the total (Figure 16, right panel), with shallow rain fractions of 12.1% and 7.4% in the EP and WP, respectively. The convective profile still peaks about 1 km higher in the WP. While the pixel counts are greater in the WP, the rain profiles are quite similar, with the EP actually overtaking the WP by a slim margin above 9 km. This leads to stratiform rain fractions of 55.6% in the EP and 49.2% in the WP.

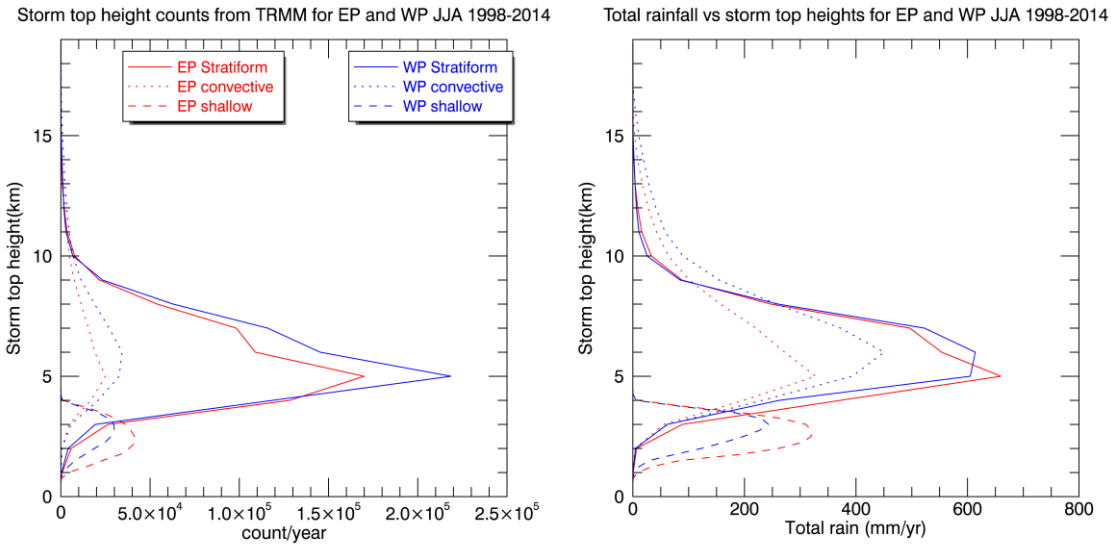

Figure 16 – Storm top height pixel counts from the TRMM PR 1998-2014 JJA climatology over the EP (red) and WP (blue) regions (left). Contribution of rainfall from different storm top heights for both regions (right). The shallow rain types have been combined together, and the other type is ignored.

The differences in the storm statistics between the EP and WP regions tend to relax during El Niño. The shapes of the rain type CFADs during El Niño years (2002, 2004, 2009; Fig. 17) are similar to climatology but with smaller difference magnitudes, especially in the convective and shallow rain types (e.g., there is 10.4% more convective echo and 37.2% less shallow echo in the WP relative to the EP). The stratiform WP-EP differences are only 1% on the whole, but again are mainly negative at higher reflectivities and 2 km where rainfall is calculated.

Storm top heights for the deep storm types during El Niño are still slightly higher in the WP (Figure 18), but the STH distributions are very similar. The shallow type STHs don't show any appreciable change from climatology. The EP produces more stratiform rain from storms of all heights, which alleviates concerns about the low-level differences in the stratiform CFADs somewhat. The convective profiles also have magnitudes that are much closer together, however, the peak is still 1 km higher in the WP. Stratiform rain fractions remain higher in the EP, at 54% versus 49.6% in the WP. There is a slightly larger difference in the shallow type rain amounts during El Niño, however the shallow rain fractions are more similar between the EP and WP (11% in the EP, 7.6% in the WP). Despite the similarities between the regions, omega profiles from reanalyses remain strongly bottom heavy in the EP (Figure 19).

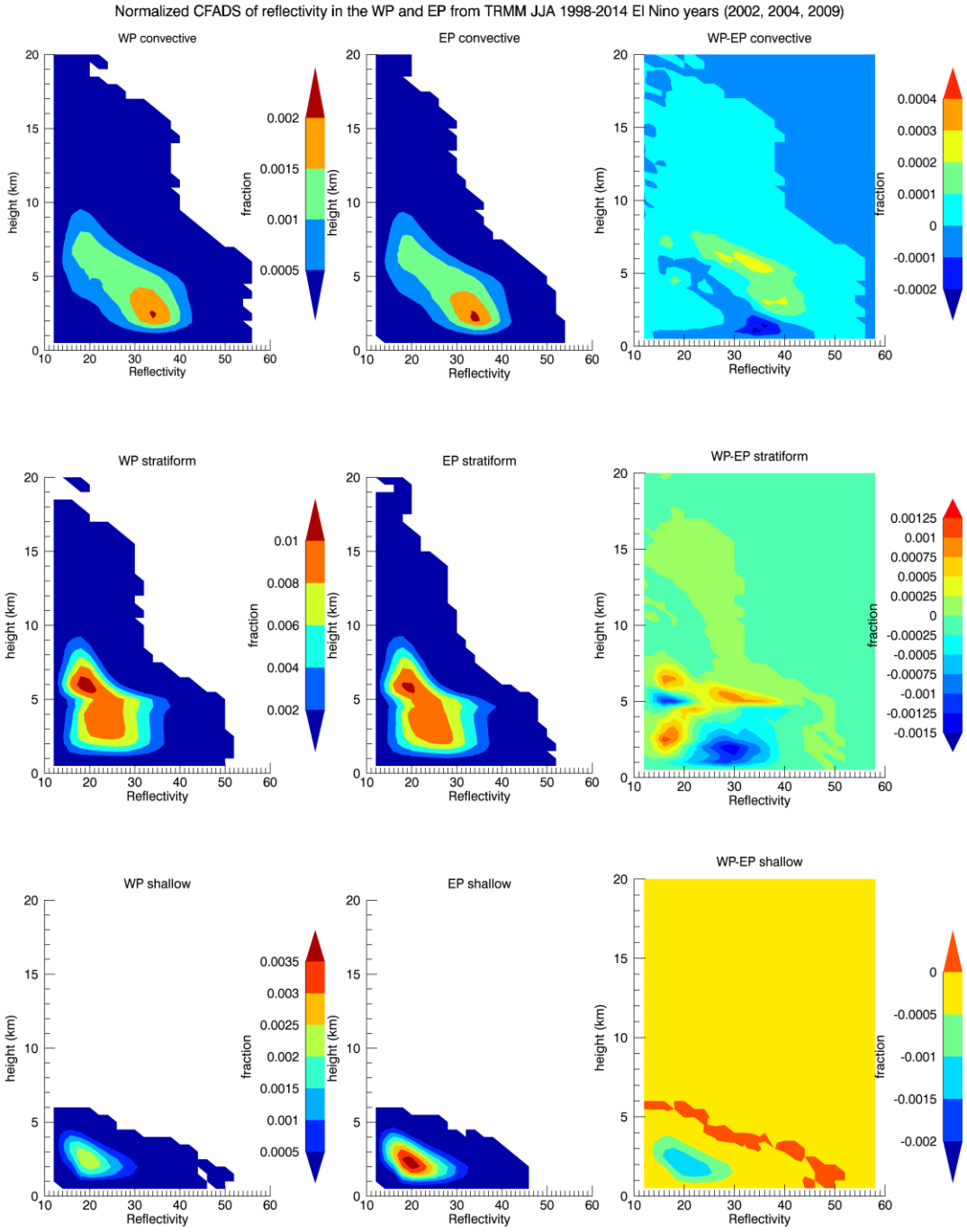

Figure 17 – Same as Figure 15, but only El Niño years (2002, 2004, 2009)

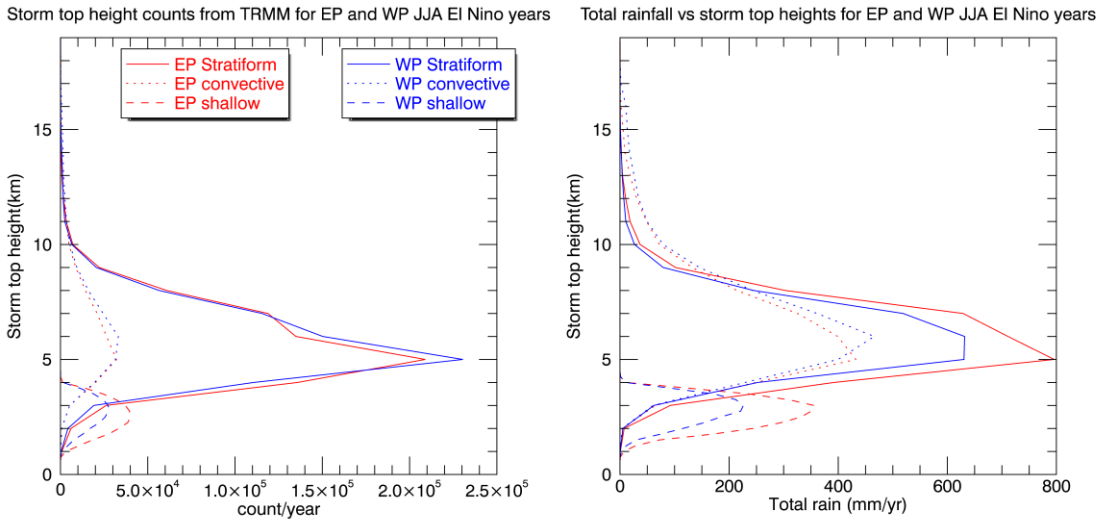

Figure 18 – Same as Figure 16, but with only El Niño years.

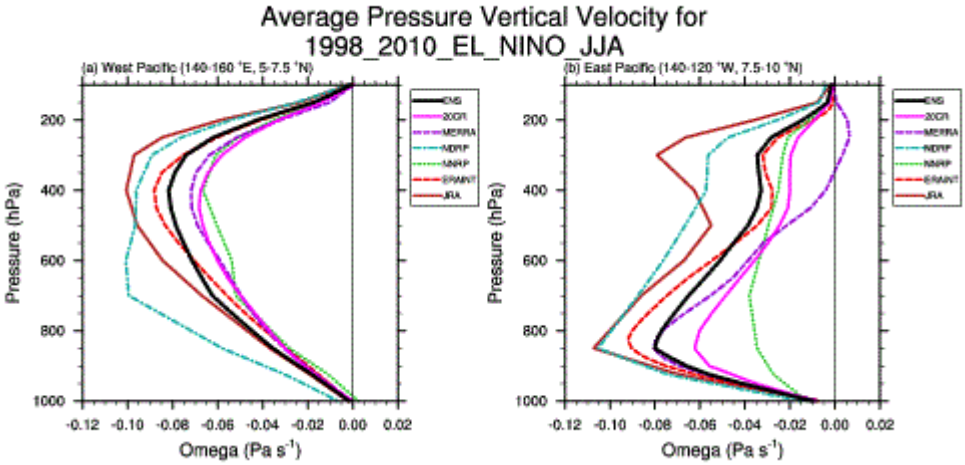

Figure 19 – Vertical profiles of omega from reanalyses and their ensemble mean in the WP (left) and EP (right) during El Niño.

If the large difference in reanalysis EP and WP omega profiles were accurate, we would expect to see larger differences in storm statistics between the regions. There would need to be a more appreciable increase in rainfall from shallow systems in the EP

relative to the WP, and much less rain from deeper systems. In fact, more rain would likely be needed from storms below 5 km than above. The observations in these regions do confirm the existence of more shallow cloud and precipitation systems and less deep convection in the EP, however the differences are subtle. There is not enough evidence to justify the reanalysis omega profiles.

Although the examined storm statistics allow us to make inferences about the resulting vertical profiles of Q_1 and ω, the point is driven home with actual latent heating calculations. As discussed in the introduction, of the numerous algorithms used for this purpose, the SLH algorithm fares best in the statistical sense. A recent study (Liu et al. 2015) used this algorithm to analyze latent heating contributions from precipitation features (PFs) of different sizes, depths, and intensities over oceanic and land regions. They specifically looked at the EP and WP, although their boxes are slightly larger than the ones used in this thesis.

Figure 20 (their Figure 9) shows contours of latent heating at different altitudes for storms with certain echo tops. Slightly lower latent heating is found in the EP where maximum heating occurs, which is between 5 and 9 km, in agreement with our echo analysis. There is also a higher magnitude of latent heating aloft in the WP from storms with 30 dBZ echo-top height between 6 and 8 km, and a lower magnitude below 3 km from storms with 30 dBZ echo tops between 1 and 5 km (Liu et al. 2015, their Fig. 12). Latent heating contributions below 4 km are only slightly higher in their EP than WP, and generally come from systems with size smaller than 1000 km^2 (their Figure 5).

However, the mean volumetric latent heating is shown to have a stronger positive peak in the EP than the WP in MCSs and in the stratiform region (their Fig. 6).

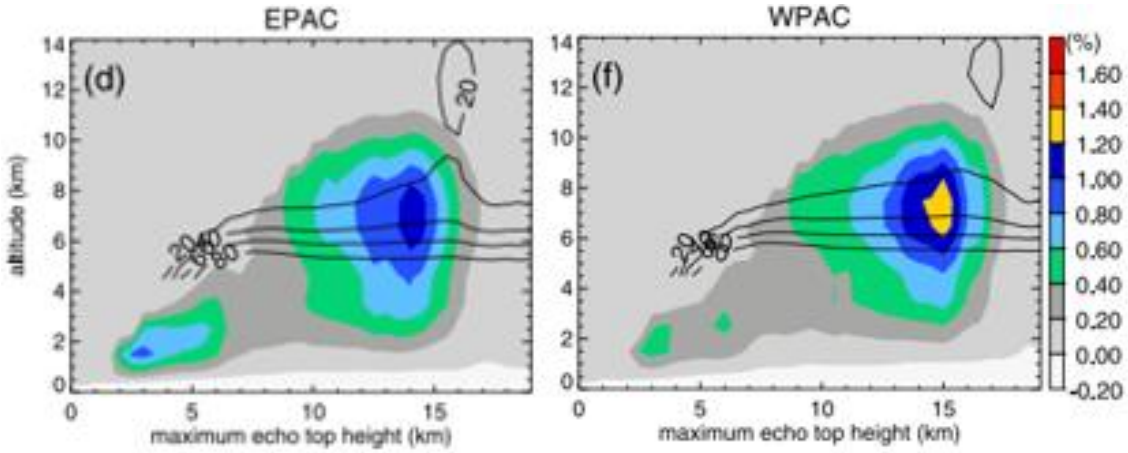

Figure 20 – Normalized contours of heating calculated by the spectral latent heating algorithm over the eastern Pacific (left) and western Pacific (right). From Liu et al. (2015)

5. FIELD CAMPAIGNS

The TEPPS campaign was the first to take extensive radar and sounding observations in the EP ITCZ. Figure 21 shows the time series of rainfall observed by the radar aboard the *RHB.* The majority of the rainfall is forced by the passage of easterly waves (solid vertical lines) and a Kelvin wave (dashed lines) that interacted with the third easterly wave. A fourth easterly wave was in progress when operations were suspended, so it could not be fully sampled.

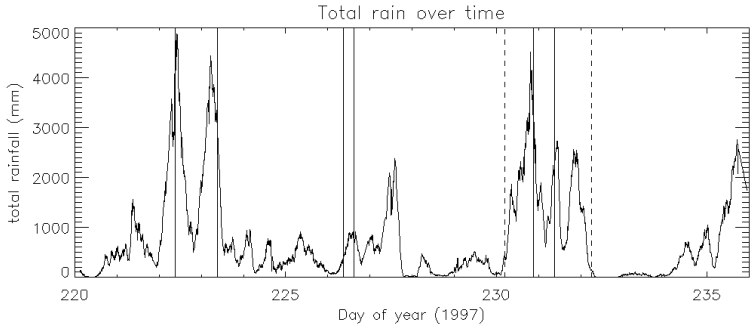

Figure 21 – Time series of total rainfall observed by the radar aboard the *RHB* during the TEPPS campaign.

Latent heating was calculated using the method of Schumacher et al. (2004) from the radar data. Before applying the idealized profiles shown in Figure 2 (left panel) convective pixels with tops above 7 km were placed into the deep category, and below 7 km into the shallow category. Due to misclassifications in the Steiner et al. (1995) algorithm, stratiform pixels with 10-dBZ echo tops below 5 km (i.e., those undergoing only warm rain processes) were re-classified as shallow convective (Schumacher and Houze 2003b). The time series and average latent heating profiles are depicted in Figure

22. In the time series (top panel) the rainy periods begin with a strongly convective heating profile from 2 to 11 km, maximizing between 2 and 2.5 K/day. Over the course of 6 to 12 hours this evolves into a stratiform heating profile with heating aloft and weak cooling near the surface. During periods of less rainfall, heating is lower in both magnitude and altitude. The majority of the total latent heating is provided by heavily raining systems forced by synoptic-scale waves. In the mean profile (bottom panel), there is a double peak structure near 3 and 7 km at around 0.5 K/day.

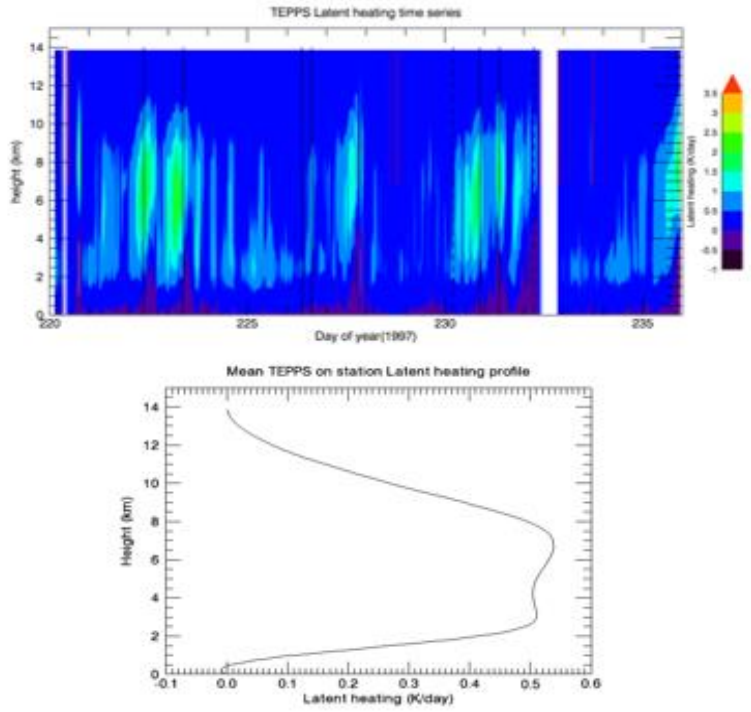

Figure 22 – Time series of latent heating calculated from the TEPPS radar data using the Schumacher et al. (2004) method (top). The mean profile of latent heating (bottom).

Vertical pressure velocities are strongly negative (upward motion) throughout much of the atmosphere in the MERRA reanalysis during the heavy rain events

associated with the first two wave passages (Figure 23, top panel). From Julian day 230 to 232, however, omega values are only weakly negative in a much smaller portion of the atmosphere, and are strongly positive at low levels on day 230 and throughout the atmosphere as the third easterly wave passed by the *RHB*. The MERRA domain (6.875 to 9.375 ºN, 124.325 to 126.875 ºW) is slightly larger than that covered by the radar, but the sensitivity to box size was investigated and results were similar.

Comparing the time series of horizontal (u, v) winds from the MERRA dataset (Figure 23, middle and bottom panels) to the sounding budget (Figure 24) gives insight into the disagreement. Zonal (u) winds remain negative (easterly) in the boundary layer in the reanalysis, whereas they often become positive in observations during periods of enhanced rainfall. During and after the passage of the Kelvin wave, weak westerlies rose from the surface into the mid-troposphere in the soundings, but the MERRA contrasts that with stronger easterlies increasing in altitude with time. Near 200 mb, the datasets are of opposite sign during most of the latter half of the on-station period, which is due to an overly strong Walker cell in the MERRA dataset in comparison with other reanalyses (see right panel of Figs. 1 and 19).

The meridional winds fare a little better in the MERRA, especially at upper levels. Surface southerlies appear during periods of rainfall as well, although many features tend to be a little bit weaker and shifted in time in both directions by up to a day. Since the sonde data has poor resolution compared to radar, the time series of VAD calculated winds are pictured in Figure 25 for comparison. The higher temporal resolution is obvious, but the patterns in both zonal and meridional winds are consistent,

even during quiescent periods. The differences between MERRA and the observations indicate that the reanalysis is poorly resolving synoptic-scale variability in the region.

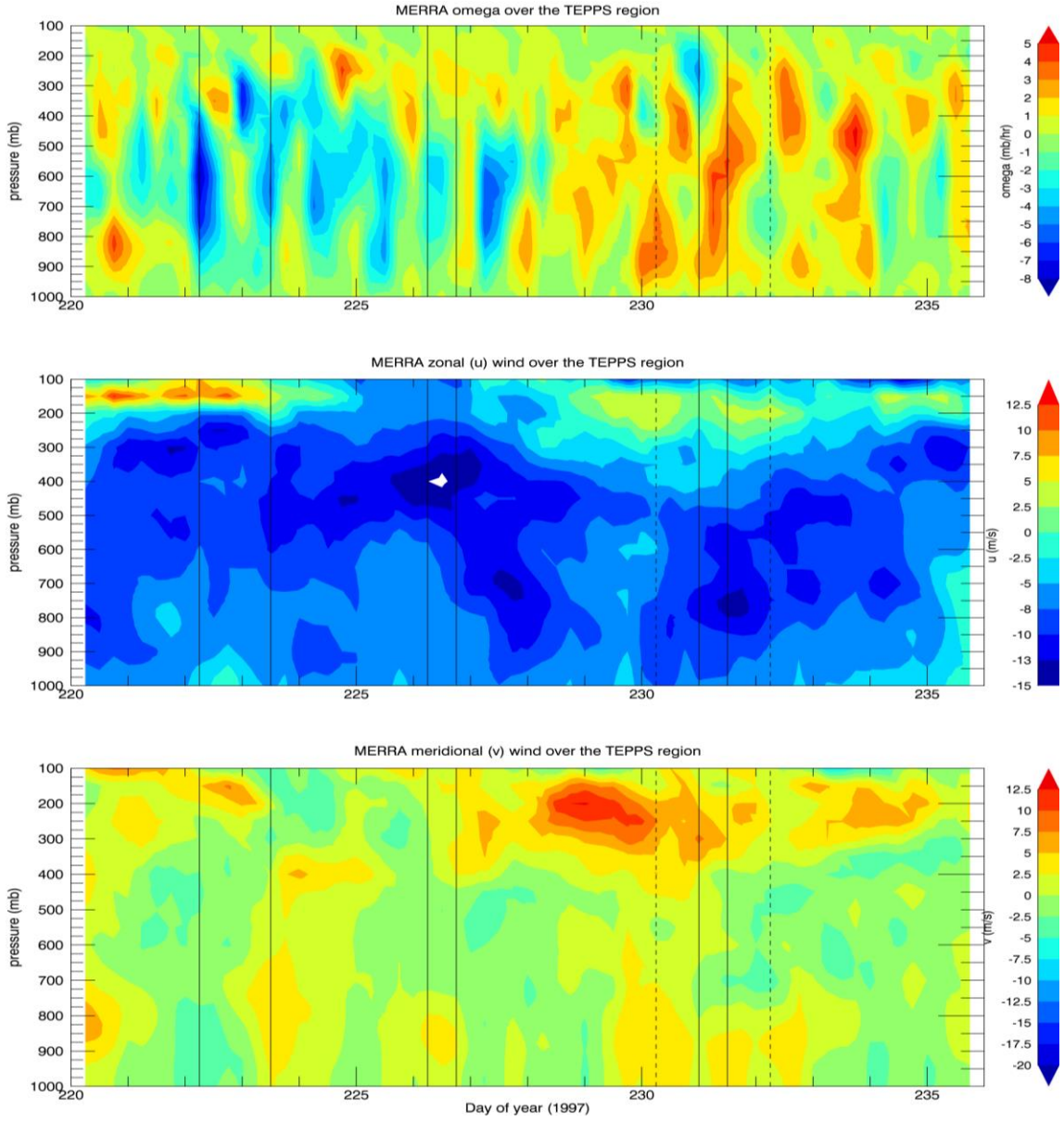

Figure 23 – Time series of ω (top), zonal winds (u; middle) and meridional winds (v; bottom) from the MERRA reanalysis over a domain lightly larger than the TEPPS *RHB* radar coverage (6.875 to 9.375 ºN, 124.325 to 126.875 ºW).

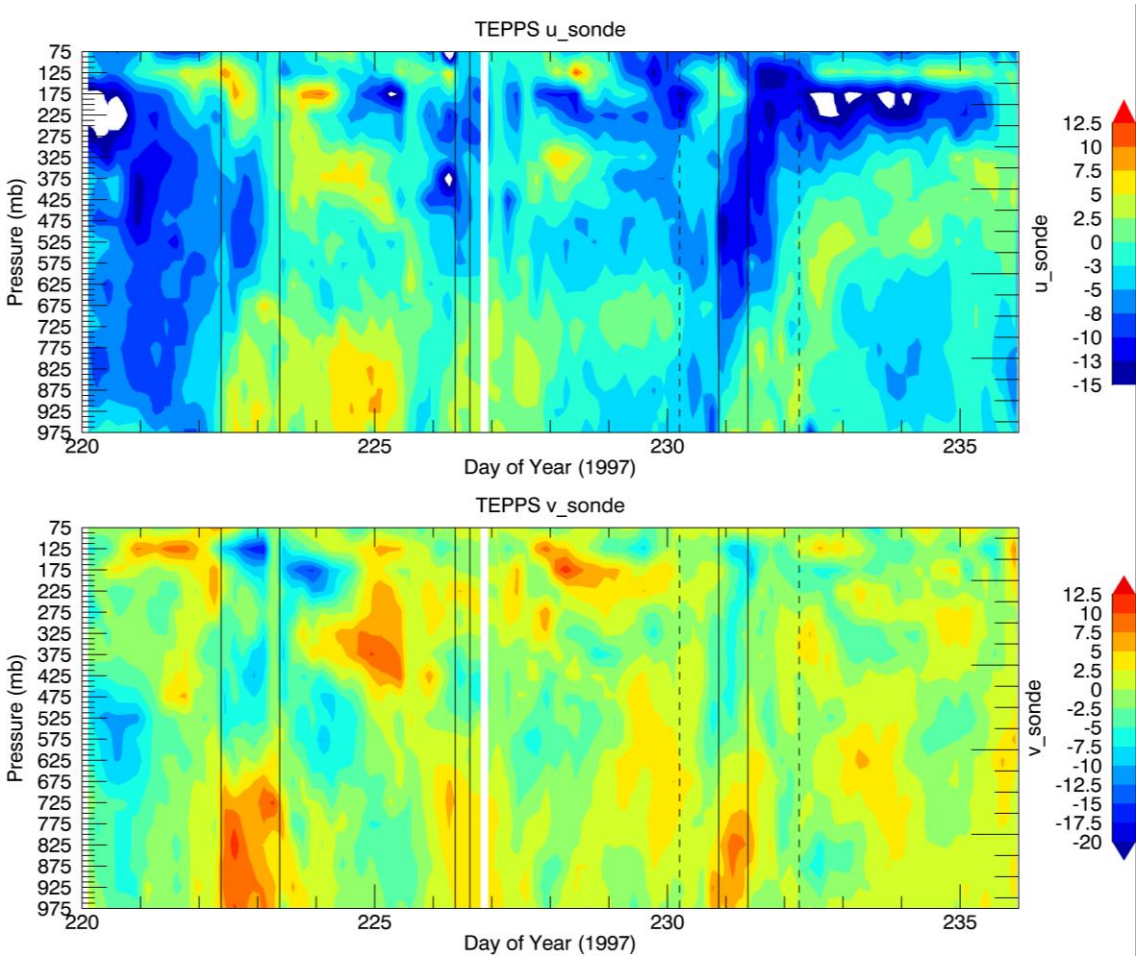

Figure 24 – Time series of zonal (u) and meridional (w) winds from TEPPS soundings.

Since the variational objective analysis was not performed on the TEPPS soundings, we will look at other datasets across the tropical oceans that can provide a better look at heating and vertical motion. Johnson et al. (in press) plotted vertical profiles of Q_1 and ω from TOGA-COARE with stratiform rain fraction (their Figs. 6 and 11). While the relationship between these two variables is not one-to-one, they both exhibit similar properties in that they maximize between 400 and 500 hPa near stratiform rain fractions of 55%.

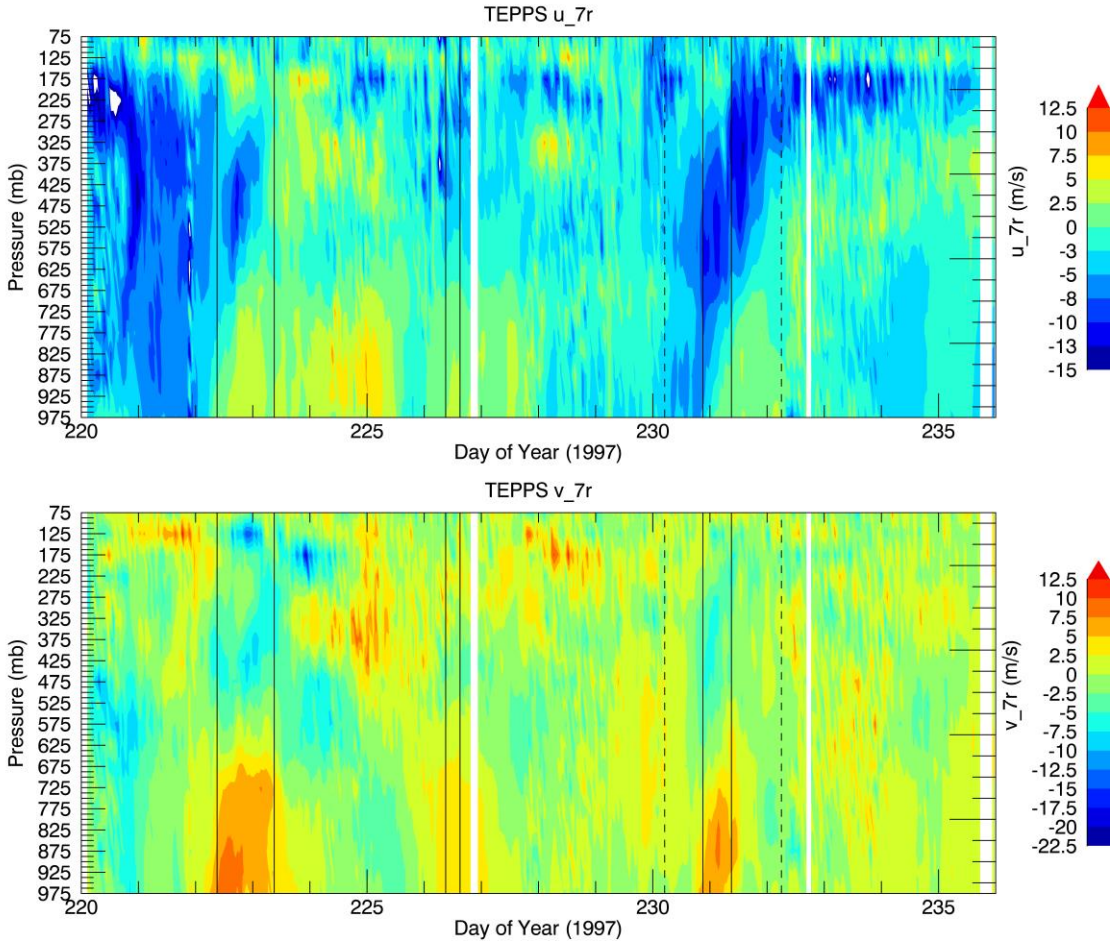

Figure 25 – Same as Figure 23, but from the VAD analysis rather than the soundings.

The TOGA-COARE dataset is from the western Pacific warm pool and had a rain threshold of 3.5 mm/day applied. So as to not lose information from lightly raining regimes, no threshold is used to plot similar relationships from the KWAJEX campaign in the central Pacific (Figure 26; left panels). The relationship between Q_1 and ω is seen regardless of the rain threshold. It is also clearer in the KWAJEX dataset that ω and Q_1increase in both height and magnitude with increasing stratiform rain fraction. The recent Dynamics of the Madden-Julian Oscillation (DYNAMO) experiment in the Indian

Ocean (0.7ºS, 73.2ºE) also exhibits these relationships (not shown), indicating some ubiquity across the tropical oceans.

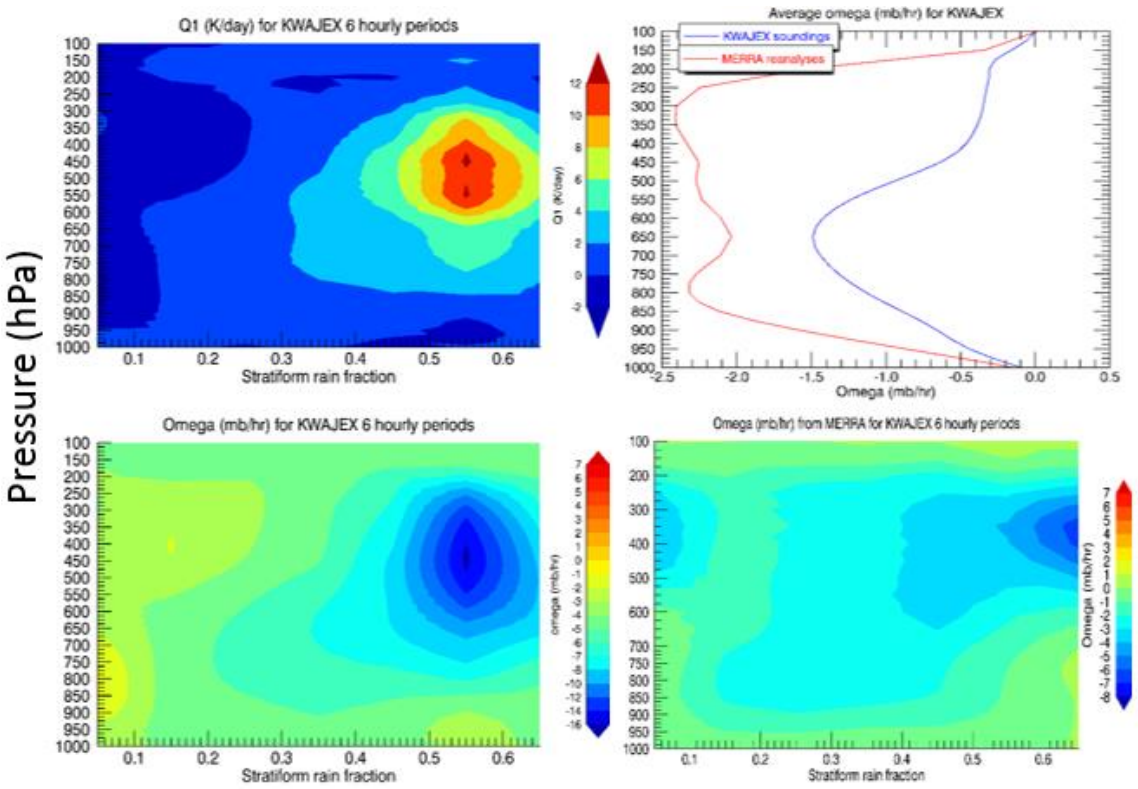

Figure 26 – Contours of Q_1 and ω from KWAJEX soundings in relation to pressure and stratiform rain fraction (left panels). Similar ω plot using MERRA data (bottom right), and the mean ω profiles from each dataset (top right).

Replacing ω with that from the MERRA dataset over a similar domain (6.875 to 9.375ºN, 165.625 to 168.125 ºE; Figure 26 bottom right panel) shows poor performance, with more bottom heavy ω at low stratiform rain fractions, and a higher peak than the soundings at high stratiform rain fractions. The mean profiles of both MERRA and sounding ω are compared as well (top right panel), and the sounding values peak near

600 mb, in good agreement with Hagos (2010) Figure 6d. In contrast, the MERRA ω has a peak near 800 hPa and a secondary upper level peak at 300-350 hPa not seen in the soundings. The strong upper level MERRA ω may be in association with the overly strong Walker cell at upper levels in the MERRA, as it is the only reanalysis with downward motion in the upper troposphere in the EP mean (Figure 1; right panel). At lower levels in the EP, the MERRA is closer to the ensemble average.

6. CONCLUSIONS

Obtaining observations of precipitation across the tropics has greatly improved our understanding of the physical processes that occur there. Despite this, there is still considerable uncertainty in the literature regarding causality; does latent heating from hydrometeor formation force circulations, or do the circulations have a greater effect on the formation of precipitation systems?

Better observations of precipitation in the tropics and midlatitudes will continue from GPM for at least the next decade by most fuel estimates. While the low-reflectivity improvements in the GPM K_u-only data are impressive, adjustments to the algorithms will be necessary to fully utilize the suite of DPR measurements. Attenuation correction in the K_a-band and DPR convective/stratiform partitioning are two of the more pressing issues. Having a period of overlap between the TRMM and GPM satellites for comparative study has been a great benefit, and plans are in place to apply the improved DPR algorithms to the TRMM dataset. This forthcoming TRMM Version 8 algorithm (due in 2017) will help create a continuous dataset across both satellites that will improve our knowledge of worldwide rainfall climatology.

Further work in the identification of stratiform rain areas from the PR and DPR is also necessary. The creation of two separate stratiform categories has been discussed as a possibility in order to differentiate between the more canonical MCS stratiform areas and the pulse-like stratiform areas discussed in Houze et al. (2015). Given the more frequent occurrence of rain of this type in the EP, this would likely bring satellite latent heating estimates down in the atmosphere slightly.

Observations of precipitation systems in the tropical Pacific have confirmed previously known differences between the EP and WP regions. The WP warm pool produces more deep convection and less shallow rain than the EP, but the differences are not as stark as those in the reanalysis profiles of vertical motion. Latent heating in these regions calculated using the SLH algorithm (Liu et al. 2015) is quite similar as well. The much larger variability between reanalyses in the sparse data region of the EP compared to the data rich WP is an indication of inaccuracies in the parameterizations.

Field campaigns across the tropical oceans demonstrate an increase in height and magnitude of observed values of both Q_1 and ω with increasing stratiform rain fraction. Direct comparisons of observed and MERRA ω confirm issues with the MERRA dataset. While other reanalyses have been shown to do well with ENSO variability, sub-seasonal variability isn't represented well. (Mo and Higgins, 1996). Synoptic variability is similarly not accurately captured in the MERRA, as shown by the time series in Figures 22 – 24. MERRA also suffers from an overly strong Walker cell.

Peaks in ω appear even lower in the CCM3 GCM than in reanalyses (Nigam et al. 2000). Since reanalyses are model based but do assimilate some observations, this is further indication of model deficiency. The true peaks in the profiles of Q_1 and ω in the EP likely lie somewhere in between the satellite and reanalysis estimates, though a secondary low level peak would likely be seen as well. A more accurate profile can be computed in the future by combining higher sensitivity GPM and CloudSat data to include more low-reflectivity echo, but a more extensive field campaign in the region is

also needed to help flesh out interactions between precipitation systems and the shallow meridional circulations and Hadley and Walker cells.

REFERENCES

Awaka, J., T. Iguchi, H. Kumagai, and K. Okamoto, 1997: Rain type classification algorithm for TRMM precipitation radar. International Geoscience and Remote Sensing Symposium, *IEEE*, Singapore, Japan, 1633-1635.

Awaka, J., T. Iguchi, and K. Okamoto, 2007: Rain Type Classification Algorithm. Measuring Precipitation from Space. EURAINAST and the Future. Levizzani, V., P. Bauer, and F. J. Turk (eds.), *Springer*, 213-224.

Awaka, J., T. Iguchi, and K. Okamoto, 2009: TRMM PR standard algorithm 2A23 and its performance on bright band detection. *J. Meteor. Soc. Japan*, **87**, 3152.

Back, L. E., and C. S. Bretherton, 2006: Geographic variability in the export of moist static energy and vertical motion profiles in the tropical Pacific. *Geophys. Res. Lett*., **33**, L17810, doi:10.1029/2006GL026672

Back, L. E., and C. S. Bretherton, 2009: On the relationship between SST gradients, boundary layer winds, and convergence over the tropical oceans. *J. Climate*, **22**, 4182-4196.

Berg, W., C. Kummerow, and C. Morales, 2002: Differences between east and west Pacific rainfall systems. *J. Climate*, **15**, 3659-3672.

Chan, S. C., and S. Nigam, 2009: Residual diagnosis of diabatic heating from ERA-40 and NCEP reanalyses: Intercomparisons with TRMM. *J. Climate*, **22**, 414-428.

Cifelli, R., S. W. Nesbitt, S. A. Rutledge, W. A. Petersen, and S. Yuter, 2007: Radar characteristics of precipitation features in the EPIC and TEPPS regions of the east Pacific. *Mon. Wea. Rev.*, **135**, 1576-1595.

Compo, G. P., et al., 2011: The twentieth century reanalysis project. *Q. J. R. Meteorol. Soc*., **137**, 1-28.

Dee, D. P., and S. Uppala, 2009: Variational bias correction of satellite radiance data in the ERA-Interim reanalysis. *Q. J. R. Meteorol. Soc*., **135**, 1830-1841.

Funk, A., C. Schumacher, and J. Awaka, 2013: Analysis of rain classifications over the tropics by version 7 of the TRMM PR 2A23 algorithm. *J. Met. Soc. Japan*, **91**, 257-272.

Grecu, M., S. Olson, C.-L. Shie, T. S. L'Ecuyer, and W.-K. Tao, 2009: Combining satellite microwave radiometer and radar observations to estimate atmospheric heating profiles. *J. Climate*, **22**, 6356-6376.

Hagos, S., 2010: Building blocks of tropical diabatic heating. *J. Atmos. Sci*., **67**, 2341-2354.

Hagos, S., C. Zhang, W.-K. Tao, S. Lang, Y. N. Takayabu, S. Shige, M. Katsumata, B. Olson, and T. L'Ecuyer, 2010: Estimates of tropical diabatic heating profiles: commonalities and uncertainties. *J. Climate*, **23**, 542-558.

Hirose, M., and K. Nakamura, 2004: Spatio-temporal variation of the vertical gradient of vertical rainfall rate observed by the TRMM precipitation radar, *J. Clim*., **17**, 3378-3397.

Hirose, M., S. Shimizu, R. Oki, T. Iguchi, D. A. Short, and K. Nakamura, 2012: Incidence-angle dependency of TRMM PR rain estimates. *J. Atmos. Oceanic Technol*., **29**, 192-206, doi:10.1175/ JTECH-D-11-00067.1.

Hou, A. Y., et al., 2014: The Global Precipitation Measurement (GPM) Mission. *Bull. Amer. Meteor. Soc.*, **95**, 701-722, doi:10.1175/BAMS -D-13-00164.1

Houze, R. A., Jr., 1982: Cloud clusters and large-scale vertical motions in the tropics. *J. Meteor. Soc. Japan,* **60**, 396-410.

Houze, R. A., Jr., 1993: *Cloud dynamics.* Academic Press, 573 pp.

Houze, R. A., Jr., 1997: Stratiform precipitation in regions of convection: A meteorological paradox? *Bull. Amer. Meteor. Soc.,* **78**, 2179-2196.

Houze, R. A., Jr., K. L. Rasmussen, M. D. Zuluaga, and S. R. Brodzik, 2015: The variable nature of convection in the tropics and subtropics: A legacy of 16 years of the Tropical Rainfall Measuring Mission (TRMM) satellite. *Rev. Geophys.*, **in press**.

Johnson, R. H., P. E. Ciesielski, and T. M. Rickenbach, 2014: A further look at Q1 and Q2 from TOGA COARE. AMS Monograph Tribute to Michio Yanai, **in press**.

Kalnay, E., et al., 1996: The NCEP/NCAR 40 year reanalysis project. *Bull. Am. Meteorol. Soc*., **77**, 437-471.

Kanamitsu, M., W. Ebisuzaki, J. Woollen, S.K. Yang, J. J. Hnilo, M. Fiorino, and G. L. Potter, 2002: NCEP/DOE AMIPII reanalysis (R2). *Bull. Am. Meteorol. Soc.*, **83**, 1631-1643.

Kim, D., M-I. Lee, D. Kim, S. D. Schubert, D. E. Waliser, and B. J. Tian, 2014: Representation of tropical subseasonal variability of precipitation in global reanalyses. *Clim. Dyn*., **43,** 517-534, doi 10. 1007/s00382-013-1890-x.

Kim, J., and M. J. Alexander, 2013: Tropical precipitation variability and convectively coupled equatorial waves on submonthly time scales in reanalyses and TRMM. *Journal of Climate*, **26**, 3013-3030.

Kubar, T. L., and D. L. Hartmann, 2008: The vertical structure of tropical oceanic convective clouds and its relation to precipitation. *Geophys. Res. Lett*., **35**, L03804, doi:10.1029/2007GL032811.

Kubota, T., N. Yoshida, S. Urita, T. Iguchi, S. Seto, R. Meneghini, J. Awaka, H. Hanado, S. Kida, and R. Oki, 2014: Evaluation of precipitation estimates by at-launch codes of GPM/DPR algorithms using synthetic data from TRMM/PR observations," *IEEE J. Sel. Topics Appl. Earth Observ. Remote Sens.*, **7**, 3931-3944. doi: 10.1109/JSTARS.2014.2320960

Le, M. and V. Chandrasekar, 2014: An algorithm for drop-size distribution retrieval from GPM dual-frequency precipitation radar. *IEEE T. Geoscience and Remote Sensing*, **52**: 7170-7185

Liao, L., R. Meneghini, and T. Iguchi, 2001: Comparisons of rain rate and reflectivity factor derived from the TRMM Precipitation Radar and the WSR-88D over the Melbourne, Florida site. *J. Atmos. Oceanic Technol*., **18**, 1959-1974.

Lindzen, R. S., and S. Nigam, 1987: On the role of sea surface temperature gradients in forcing low level winds and convergence in the tropics. *J. Atmos. Sci*., **44**, 2418-2436.

Ling, J., and C. Zhang, 2013: Diabatic heating profiles in recent global reanalyses. *J. Climate*, 26, 3307-3325.

Liu, C., and E. J. Zipser, 2013: Why does radar reflectivity tend to increase downward toward the ocean surface, but decrease downward toward the land surface?, *J. Geophys. Res. Atmos*. **118**, 135-148, doi:10.1029/2012JD018134

Liu C., S. Shige, Y. N. Takayabu, and E. Zipser, 2015: Latent Heating Contribution from Precipitation Systems with Different Sizes, Depths, and Intensities in the Tropics. *J. Climate*, **28**, 186-203. doi: http://dx.doi.org/10.1175/JCLI-D-14-00370.1

Mapes, B. E., and J. Lin, 2005: Doppler radar observations of mesoscale wind divergence in regions of tropical convection. *Mon. Wea. Rev*., **133**, 1808–1824.

Mapes, B. E., and R. A**.** Houze, Jr., 1995: Diabatic divergence profiles in western Pacific mesoscale convective systems. *J. Atmos. Sci.*, **52**, 1807-1828.

Mapes, B. E., S. Tulich, J.-L. Lin, and P. Zuidema, 2006: The mesoscale convection life cycle: building block or prototype for large-scale tropical waves? *Dyn. Atmos. Oceans*, **42**, 3-29.

Masunaga, H., T. S. L'Ecuyer, and C. D. Kummerow, 2005: Variability in the characteristics of precipitation systems in the tropical Pacific. Part I: spatial structure. *J. Climate*, **18**, 823-840.

Mo, K. C., and R. W. Higgins, 1996: Large-scale atmospheric water vapor transport as evaluated from the NCEP/NCAR and the NASA/ DAO reanalyses. *J. Climate*, **9**, 1531-1545.

Nesbitt, S. W., E. J. Zipser, and D. J. Cecil, 2000: A census of precipitation features in the Tropics using TRMM: Radar, ice scattering, and lightning observations. *J. Climate*, **13**, 4087-4106

Nigam, S., and C. Chung, 2000: ENSO surface winds in CCM3 Simulation:Diagnosis of errors. *J. Climate*, **13**, 3172-3186.

Nigam, S., C. Chung, and E. DeWeaver, 2000: ENSO diabatic heating in ECMWF and NCEP–NCAR reanalyses, and NCAR CCM3 simulation. *J. Climate*, **13**, 3152-3171.

Nitta, T., and S. Esbensen, 1974: Heat and Moisture Budget Analyses Using BOMEX Data. *Mon. Wea. Rev.*, **102**, 17-28. doi: http://dx.doi.org/10.1175/1520-0493(1974)102<0017:HAMBAU>2.0.CO;2

Nolan, D. S., C. Zhang, and S. Chen, 2007: Dynamics of the Shallow Meridional Circulation around Intertropical Convergence Zones. *J. Atmos. Sci*, 64, 2262-2285.

Onogi, K., J. Tsutsui, H. Koide, M. Sakamoto, S. Kobayashi, H. Hatsushika, T. Matsumoto, N. Yamazaki, H. Kamahori, K. Takahashi, S. Kadokura, K. Wada, K. Kato, R. Oyama, T. Ose, N. Mannoji, and R. Taira, 2007: The JRA25 reanalysis. *J. Meteorol. Soc. Jpn*., **85**, 369-432.

Petersen, W. A., R. Cifelli, D. J. Boccippio, S. A. Rutledge, and C. Fairall, 2003: Convection and easterly wave structures observed in the eastern Pacific warm pool during EPIC--2001. *J. Atmos. Sci*., **60**, 1754-1773

Pfeifroth, U., R. Mueller, and B. Ahrens, 2013: Evaluation of satellite-based and reanalysis precipitation data in the tropical Pacific. *J. Appl. Meteor. Climatol.*, **52**, 634-644.

Raymond, D. J., et al., 2004: EPIC2001 and the coupled ocean–atmosphere system of the tropical east Pacific. *Bull. Amer. Meteor. Soc.*, **85**, 1341-1354

Roca, R., J. Aublanc, P. Chambon, T. Fiolleau, and N. Viltard, 2014: Robust Observational Quantification of the Contribution of Mesoscale Convective Systems to Rainfall in the Tropics. *J. Climate*, **27**, 4952-4958. doi: http://dx.doi.org/10.1175/JCLI-D-13-00628.1

Rienecker, M. M., et al., 2011: MERRA: NASA's modernera retrospective analysis for research and applications. *J. Climate*., **24**, 3624-3648.

Saha, S., et al., 2010: The NCEP climate forecast system reanalysis. *Bull. Am. Meteorol. Soc*., **91**, 1015–1057.

Schumacher, C., M. H. Zhang, and P. E. Ciesielski, 2007: Heating structures of the TRMM field campaigns. *J. Atmos. Sci*., **64**, 2593-2610.

Schumacher, C., P. E. Ciesielski, and M. H. Zhang, 2008: Tropical Cloud Heating Profiles: Analysis from KWAJEX. *Mon. Wea. Rev.*,**136**, 4289-4300. doi: http://dx.doi.org/10.1175/2008MWR2275.1

Schumacher, C., and R. A. Houze Jr., 2000: Comparison of radar data from the TRMM satellite and Kwajalein oceanic validation site. *J. Appl. Meteor.*, **39**, 2151-2164

Schumacher, C., and R. A. Houze, Jr., 2003a: Stratiform rain in the tropics as seen by the TRMM Precipitation Radar. *J. Climate*, **16**, 1739-1756.

Schumacher, C., and R. A. Houze, Jr., 2003b: The TRMM Precipitation Radar's view of shallow, isolated rain. *J. Appl. Meteor.*, **42**, 1519-1524.

Schumacher, C., R. A. Houze, Jr., and I. Kraucunas, 2004: The Tropical dynamical response to latent heating estimates derived from the TRMM precipitation radar. *J. Atmos. Sci*., **61**, 1341-1358

Sherwood, S. C., S. Bony and J.-L. Dufresne, 2014: Spread in model climate sensitivity traced to atmospheric convective mixing. *Nature*, **505**, 37-42.

Shige, S., T. Watanabe, H. Sasaki, T. Kubota, S. Kida, and K. Okamoto, 2008b: Validation of western and eastern Pacific rainfall estimates from the TRMM PR using a radiative transfer model. *J. Geophys. Res*., **113**, D15116, doi:10.1029/2007JD009002

Shige, S., Y. N. Takayabu, W.-K. Tao, and D. E. Johnson, 2004: Spectral retrieval of latent-heating profiles from TRMM PR data. Part I: Development of a model-based algorithm. *J. Appl. Meteor.,* **43**, 1095-1113.

Shige, S., Y. N. Takayabu, W.-K. Tao, and C.-L. Shie, 2007: Spectral retrieval of latent-heating profiles from TRMM PR data. Part II: Algoritm improvement and heating estimates over tropical ocean regions. *J. Appl. Meteor. Climatol.,* **46**, 1098-1124.

Shige, S., Y. N. Takayabu, and W.-K. Tao, 2008a: Spectral retrieval of latent heating profiles from TRMM PR data. Part III: Estimating apparent moisture sink profiles over tropical oceans. *J. Appl. Meteor. Climatol.*, **47**, 620-640.

Shige, S., Y. N. Takayabu, S. Kida, W.-K. Tao, X. Zeng, C. Yokoyama, and T. L'Ecuyer, 2009: Spectral retrieval of latent heating profiles from TRMM PR data. Part IV: Comparisons of lookup tables from two- and three-dimensional simulations. *J. Climate*, **22**, 5577-5594

Shimizu, S., N. Takahashi, T. Iguchi, J. Awaka, T. Kozu, R. Meneghini, and K. Okamoto, 2003: Validation analyses after the altitude change of TRMM. *Proc. SPIE*, **4894**, 83-91.

Shimizu, S., R. Oki, T. Tagawa, T. Iguchi, and M. Hirose, 2009: Evaluation of the effects of the orbit boost of the TRMM satellite on PR rain estimates, *J. Meteor. Soc. Japan.*, **87A**, 83-92, doi:10.2151/jmsj.87A.83.

Stachnik, J. P., and C. Schumacher, 2011: A comparison of the Hadley circulation in modern reanalyses. *J. Geophys. Res*., **116**, D22102, doi:10.1029/2011JD016677.

Stachnik, J. P., C. Schumacher, and P. E. Ciesielski, 2013: Total Heating Characteristics of the ISCCP Tropical and Subtropical Cloud Regimes. *J. Climate*, **26**, 7097-7116. doi: http://dx.doi.org/10.1175/JCLI-D-12-00673.1

Steiner, M., R. A. Houze, Jr., and S. E. Yuter, 1995: Climatological characterization of three-dimensional storm structure from operational radar and rain guage data. *J. Appl. Meteor.*, **34,** 1978-2007

Straub, K. H., and G. N. Kiladis, 2002: Observations of a convectively coupled Kelvin wave in the eastern Pacific ITCZ, *J. Climate*, **2**, 1492-1499

Tao, W.-K., S. Lang, J. Simpson, and R. Adler, 1993: Retrieval algorithms for estimating the vertical profiles of latent heat release: Their applications for TRMM. *J. Meteor. Soc. Japan*, **71**, 685-700

Tao, W.-K., S. Lang, X. Zeng, S. Shige, and Y. Takayabu, 2010: Relating convective and stratiform rain to latent heating. *J. Climate*, **23**, 1874-1893

Tao, W.-K., et al., 2001: Retrieved vertical profiles of latent heating release using TRMM rainfall products for February 1998. *J. Appl. Meteor*., **40**, 957-982.

Tao, W.-K., et al., 2006: Retrieval of latent heating from TRMM measurements. *Bull. Amer. Meteor. Soc.*, **87**, 1555-1572.

Toyoshima, K., H. Masunaga, and F. A. Furuzawa, 2015: Early evaluation of K_u- and K_a-band sensitivities for the Global Precipitation Measurement (GPM) dual-frequency precipitation radar (DPR). *SOLA*, **11**, 14-17.

Trenberth, K. E., D. P. Stepaniak, and J. M. Caron, 2000: The global monsoon as seen through the divergent atmospheric circulation. *J. Climate*, **13**, 3969-3993.

TRMM PR Team, 2011: Tropical Rainfall Measuring Mission (TRMM) precipitation radar algorithm Instruction Manual for Version 7. JAXA-NASA, 170 pp. [Available online at http://www.eorc.jaxa.jp/TRMM/documents/PR_algorithm_product_information/pr_manual/PR_Instruction_Manual_V7_L1.pdf.]

Uppala, S. M., et al., 2005: The ERA40 reanalysis. *Q. J. R. Meteorol. Soc*., **131**, 2961-3012.

Waliser, D. E., J. A. Ridout, S. Xie, and M. Zhang, 2002: Variational Objective Analysis for Atmospheric Field Programs: A Model Assessment. *J. Atmos. Sci.*, **59**, 3436-3456. doi: http://dx.doi.org/10.1175/1520-0469(2002)059<3436:VOAFAF>2.0.CO;2

Webster, P. J. and R. Lukas, 1992: TOGA COARE: The coupled ocean-atmosphere response 344 experiment. *Bull. Amer. Meteor. Soc*., **73**, 1377-1416.

Wong, S., T. L'Ecuyer, W. S. Olson, X. Jiang, and E. J. Fetzer, 2014: Local balance and variability of atmospheric heat budget over oceans: Observation and reanalysis-based estimates. *J. Climate*, **27**, 893-913

Yanai, M., S. Esbensen, and J. H. Chu, 1973: Determination of bulk properties of tropical cloud clusters from large-scale heat and moisture budgets. *J. Atmos. Sci.*, **30**,

611-627.

Yokoyama, C., E. J. Zipzer, and C. Liu, 2014: TRMM-observed shallow vs deep convection in the eastern Pacific related to large-scale circulations in reanalysis datasets. *J. Climate,* **27**, 5575-5591.

Yokoyama, C., and Y. N. Takayabu, 2012: Relationships between rain characteristics and Environment. Part I: TRMM precipitation features and the large-scale environment over the tropical Pacific. *Mon. Wea. Rev*, **140**, 2831-2840.

Yuter, S. E., and R. A. Houze Jr., 1995: Three-dimensional kinematic and microphysical evolution of Florida cumulonimbus. Part II: frequency distributions of vertical velocity, reflectivity, and differential reflectivity. *Mon. Wea. Rev.*, **123**, 1941-1963.

Yuter, S. E., and R. A. Houze Jr., 2000: The 1997 Pan American Climate Studies Tropical Eastern Pacific Process Study. Part I: ITCZ region. *Bull. Amer. Meteor. Soc*., **81**, 451-481.

Yuter, S. E., R. A. Houze Jr., E. A. Smith, T. T. Wilheit, and E. Zipser, 2005: Physical characterization of tropical oceanic convection observed in KWAJEX. *J. Appl. Meteor.*, **44**, 385-415.

Zhang, C., D. S. Nolan, C. D. Thorncroft, and H. Nguyen 2008: Shallow meridional circulations in the tropical atmosphere. *J. Climate*, **21**, 3453-3470.

Zhang, M. H., and J. L. Lin, 1997: Constrained variational analysis of sounding data based on column-integrated budgets of mass, heat, moisture, and momentum: Approach and application to ARM measurements. *J. Atmos. Sci.*, **54**, 1503-1524

Zhang, C., M. McGauley, and N. Bond, 2004: Shallow meridional circulation in the tropical eastern Pacific. *J. Climate*, **17**, 133-139.

Zhang, C., and S. M. Hagos, 2009: Bi-modal structure and variability of large-scale diabatic heating in the tropics. *J. Atmos. Sci*., **66**, 3621-3640